

1 **Insights into carbonate environmental conditions in the Chukchi Sea**

2

3 Claudine Hauri¹, Brita Irving¹, Sam Dupont^{2,3}, Rémi Pagés¹, Donna D. W. Hauser¹, and Seth L.

4 Danielson⁴

5

6 ¹ International Arctic Research Center, University of Alaska Fairbanks, Fairbanks, AK 99775,

7 USA

8 ² Department of Biological and Environmental Sciences, University of Gothenburg,

9 Fiskebäckskil 45178, Sweden

10 ³ Radioecology Laboratory International Atomic Energy Agency (IAEA), Marine Laboratories,

11 Principality of Monaco

12 ⁴ College of Fisheries and Ocean Science, University of Alaska Fairbanks, Fairbanks, AK 99775,

13 USA

14

15 Correspondence email: chauri@alaska.edu

16 **Abstract**

17 Healthy Arctic marine ecosystems are essential to the food security and sovereignty, culture,
18 and wellbeing of Indigenous Peoples in the Arctic. At the same time, Arctic marine ecosystems
19 are highly susceptible to impacts of climate change and ocean acidification. While increasing
20 ocean and air temperatures and melting sea ice act as direct stressors on the ecosystem, they also
21 indirectly enhance ocean acidification, accelerating the associated changes in the inorganic
22 carbon system. Yet, much is to be learned about the current state and variability of the inorganic
23 carbon system in remote, high-latitude oceans. Here, we present time-series (2016-2020) of pH
24 and the partial pressure of carbon dioxide ($p\text{CO}_2$) from the northeast Chukchi Sea continental
25 shelf. The Chukchi Ecosystem Observatory includes a suite of subsurface year-round moorings
26 sited amid a biological hotspot that is characterized by high primary productivity and a rich
27 benthic food web that in turn supports coastal Inupiat, whales, ice seals, walrus (*Odobenus*
28 *rosmarus*), and Arctic cod (*Boreogadus saida*). Our observations suggest that near-bottom
29 waters (33 m depth, 13 m above the seafloor) are a high carbon dioxide and low pH and
30 aragonite saturation state (Ω_{arag}) environment in summer and fall, when organic material from the
31 highly productive summer remineralizes. During this time, Ω_{arag} can be as low as 0.4. In winter,
32 when the site was covered by sea ice, pH was < 8 and Ω_{arag} remained undersaturated under the
33 sea ice. There were only two short seasonal periods with relatively higher pH and Ω_{arag} , which
34 we term ocean acidification relaxation events. In spring, high primary production from sea ice
35 algae and phytoplankton blooms led to spikes in pH ($\text{pH} > 8$) and aragonite oversaturation. In
36 late fall, strong wind-driven mixing events that delivered low CO_2 surface water to the shelf also
37 led to events with elevated pH and Ω_{arag} . Given the recent observations of high rates of ocean
38 acidification, and sudden and dramatic shift of the physical, biogeochemical, and ecosystem

Deleted:

40 conditions in the Chukchi Sea, it is possible that the observed extreme conditions at the Chukchi
41 Ecosystem Observatory are deviating from carbonate conditions to which many species are
42 adapted.

43

44 **1. Introduction**

45 The quickly changing Arctic Ocean has climatic, societal, and geopolitical implications for
46 the peoples of the Arctic and beyond (Huntington et al., 2022). Arctic Indigenous Peoples are at
47 the forefront of this change and their food security, food sovereignty, culture, and ways of life
48 depend on healthy Arctic marine ecosystems (ICC, 2015). The Arctic is warming at a rate that is
49 up to four times that of the rest of the globe (Serreze and Barry, 2011; Serreze and Francis, 2006;
50 Rantanen et al., 2022). This phenomenon, called Arctic Amplification, is observed in air and sea
51 temperatures, has accelerated in recent years, and is expected to continue in the future (Rantanen
52 et al., 2022; Shu et al., 2022). Warming exerts a toll on sea ice extent, ice thickness, and the
53 duration of seasonal sea ice cover: ice is forming later in fall and retreating earlier in spring,
54 thereby increasing the length of the open water period (Stroeve et al., 2011; Serreze et al., 2016;
55 Wood et al., 2015; Stroeve et al., 2014). The lowest Arctic wide minimum sea ice extents were
56 recorded during the last 16 years of the 44 year-long satellite time-series (National Snow and Ice
57 Data Center, [DiGirolamo et al. \(2022\)](#)).

Deleted: 2017

58 At the same time, the Arctic Ocean is vulnerable to ocean acidification. Although oceanic
59 uptake of anthropogenic carbon dioxide (CO₂) increases oceanic CO₂ and decreases pH and
60 calcium carbonate (CaCO₃) saturation states of calcite (Ω_{calc}) and aragonite (Ω_{arag}) globally,
61 climate induced changes to riverine input, temperature, sea ice, and circulation are accelerating
62 the rate of ocean acidification in the Arctic Ocean like nowhere else in the world (Woosley and

64 Millero, 2020; Qi et al., 2022a; Yamamoto-Kawai et al., 2009; Orr et al., 2022; Semiletov et al.,
65 2016; Qi et al., 2017). Recent observational studies propose that freshening of the Arctic Ocean
66 due to increased riverine input may play an even greater role in acidifying the Arctic Ocean than
67 the uptake of anthropogenic CO₂ (Woosley and Millero, 2020; Semiletov et al., 2016). In
68 addition, the cold Arctic waters have naturally low concentrations of carbonate ions (CO₃²⁻) and
69 are therefore closer to aragonite undersaturation ($\Omega_{\text{arag}} < 1$) than more temperate waters (Orr,
70 2011; Sarmiento and Gruber, 2006), which leads to the chemical dissolution of free aragonitic
71 CaCO₃ structures (Bednaršek et al., 2021). Because of the naturally low concentrations of CO₃²⁻,
72 such high latitude waters have a lower capacity to take up anthropogenic CO₂ and buffer these
73 changes (Orr, 2011). As a result, concentrations of hydrogen ions (H⁺) increase and pH decreases
74 faster in the Arctic than in the tropics, for example.

75 In the Pacific Arctic, the Chukchi shelf waters have warmed by 0.45 °C decade⁻¹ since 1990,
76 triple the rate since the beginning of the data record in 1922 (Danielson et al., 2020). Direct
77 observations of the inorganic carbon dynamics of the Chukchi Sea are mostly limited to June
78 through November because of the region's remoteness and accessibility during sea ice covered
79 months. Summertime profiles across the Chukchi Sea show steep vertical gradients in inorganic
80 carbon chemistry (Bates, 2015; Bates et al., 2009; Pipko et al., 2002; Mathis and Questel, 2013).
81 Surface waters have a low partial pressure of carbon dioxide ($p\text{CO}_2$) as a result of high primary
82 production after sea ice retreat, leading to aragonite supersaturated conditions, with $\Omega_{\text{arag}} > 2$
83 (Bates, 2015; Bates et al., 2009). In areas with sea ice melt or riverine freshwater influence, Ω_{arag}
84 tends to be lower and at times undersaturated (Bates et al., 2009; Yamamoto-Kawai et al., 2009).
85 At the same time, $p\text{CO}_2$ values near the seafloor are around 1000 μatm as a result of organic
86 matter remineralization, leading to summertime aragonite undersaturation (Mathis and Questel,

87 2013; Pipko et al., 2002; Bates, 2015). Between September and November, continuous
88 measurements from within a few meters of the surface suggest a mosaic of $p\text{CO}_2$ levels between
89 ~ 200 to $600 \mu\text{atm}$, likely due to patchy wind-induced mixing entraining high- CO_2 waters from
90 depth into the surface mixed layer (Hauri et al., 2013). Yamamoto-Kawai et al. (2016) used
91 mooring observations of S, T, and apparent oxygen utilization to estimate dissolved inorganic
92 carbon (DIC), total alkalinity (TA), and Ω_{arag} in bottom waters at their mooring site in the Hope
93 Valley in the southwestern Chukchi Sea to give first insights into year round variability of the
94 inorganic carbon system. They found slightly less intense aragonite undersaturation in spring and
95 winter compared to summer, with a net undersaturation duration of 7.5-8.5 months per year.

96 The Chukchi Ecosystem Observatory (CEO) is situated in a benthic hotspot (Figure 1) where
97 high primary production supports rich and interconnected benthic and pelagic food webs
98 (Grebmeier et al., 2015; Moore and Stabeno, 2015). The benthos is dominated by calcifying
99 bivalves, polychaetes, amphipods, sipunculids, echinoderms and crustaceans (Grebmeier et al.,
100 2015; Blanchard et al., 2013). Benthic foraging bearded seals (*Erignathus barbatus*), walrus
101 (*Odobenus rosmarus divergens*), gray whale (*Eschrichtius robustus*), and seabirds feed on these
102 calcifiers during the open water season (Kuletz et al., 2015; Jay et al., 2012; Moore et al., 2022).
103 The CEO site, located on the southern flank of Hanna Shoal, is a region of reduced stratification
104 (relative to other sides of the shoal) that likely alternately feels the effects of differing flow
105 regimes located to the west and to the east (Fang et al., 2020). Consequently, the site exhibits
106 relatively weaker currents (Tian et al., 2021) and so is conducive to deposition of sinking organic
107 matter that in turn feeds the local benthos (Grebmeier et al., 2015). Prolonged open-water
108 seasons during periods of high solar irradiance, in combination with an influx of new nutrients
109 and wind mixing, are likely enhancing primary and secondary production as well as advection of

110 zooplankton (Lewis et al., 2020; Arrigo and van Dijken, 2015; Wood et al., 2015). These
111 physical processes in turn fuel keystone consumers such as Arctic cod (*Boreogadus saida*) and
112 upper trophic level ringed seals (*Phoca hispida*), beluga (*Delphinapterus leucas*) and bowhead
113 whales (*Balaena mysticetus*) as well as predatory polar bears (*Ursus arctos*) and Indigenous
114 People who rely on the marine ecosystem for traditional and customary harvesting (Huntington
115 et al., 2020).

116 Perturbation of the seawater carbonate system associated with ocean acidification and
117 climate change can have significant physiological and ecological consequences for marine
118 species and ecosystems (Doney et al., 2020). All parameters of the carbonate system (pH, $p\text{CO}_2$,
119 Ω_{arag} , concentrations of HCO_3^- , CO_3^{2-} , etc.) have the potential to affect the physiology of marine
120 organisms while a change in the saturation state (Ω) can lead to the dissolution of unprotected or
121 “free” CaCO_3 structures. Recent work has highlighted the importance of local adaptation to the
122 present environmental variability as a key factor driving species sensitivity to ocean acidification
123 (Vargas et al., 2017, 2022). As carbonate chemistry conditions vary enormously between
124 regions, marine organisms are naturally exposed to different selective pressures and can evolve
125 different strategies to cope with low pH or Ω , or high $p\text{CO}_2$. For example, the deep-sea mussel
126 *Bathymodiolus brevior* living around vents at 1600 m depths is capable of precipitating calcium
127 carbonate at pH ranging between 5.36 and 7.30 and highly undersaturated waters (Tunnicliffe et
128 al., 2009). The response to changes in the carbonate chemistry is also modulated by other
129 environmental drivers such as temperature or food availability (e.g. Thomsen et al., 2013;
130 Breitberg et al., 2015). Consequently, no absolute or single threshold is expected for ocean
131 acidification (e.g., Bednaršek et al., 2021) and a pre-requisite to assessing the impact on any
132 biota is the monitoring at a short temporal scale to characterize the present environmental niche.

133 When it comes to future impacts, the more intense and faster the changes associated with ocean
134 acidification, the more adverse associated biological impacts are expected (Vargas et al. 2017,
135 2022). As a result, it is anticipated that Arctic marine waters that are experiencing widespread
136 and rapid ocean acidification will potentially undergo severe negative ecosystem impacts
137 (AMAP 2018).

138 Here, we present satellite sea ice coverage data and four years of nearly continuous salinity,
139 temperature, and $p\text{CO}_2$ data, accompanied by pH, nitrate (NO_3), dissolved oxygen (O_2), and
140 chlorophyll fluorescence data for some of the time (Table 1, Figures 2 and 3). We developed an
141 empirical equation for estimating pH from moored $p\text{CO}_2$, temperature, and salinity and evaluated
142 it using discrete samples collected across the Chukchi Sea, Bering Sea, and Beaufort Sea. Our
143 timeseries allow us to assess the seasonal and interannual variability and controls of the
144 inorganic carbon system in the Chukchi Sea between 2016 and 2020 and characterize the
145 chemical conditions experienced by organisms. We discuss our observations in terms of
146 progressing acidification and implications to organisms in the Chukchi Sea region.

147

148 **2. Materials and Methods**

149 **2.1 The Chukchi Ecosystem Observatory (CEO)**

150 The Chukchi Sea is a shallow shelf sea with maximum depths < 50 m. It is largely a
151 unidirectional inflow shelf system with Pacific origin water entering the Chukchi Sea through the
152 Bering Strait and advecting north into the Arctic Ocean (Carmack and Wassmann, 2006). The
153 CEO ($71^\circ 36'$ N, $161^\circ 30'$ W, Figure 1, Hauri et al., 2018) is located along the pathway of waters
154 flowing through Bering Strait (Fang et al., 2020) and thence from the west of Hanna Shoal
155 toward Barrow Canyon to the south, although the wind can also drive waters from the east over

156 the observatory site (Fang et al., 2020). From both shipboard and moored acoustic Doppler
157 current profiler records, the south side of Hanna Shoal mean flow is characterized by a weak
158 southward-directed current (Tian et al., 2021).

159 The observatory consists of oceanographic moorings that sample year-round, equipped with a
160 variety of sensors that measure sea ice cover and thickness (Sandy et al., 2022), light, currents,
161 waves, salinity, temperature, concentrations of dissolved oxygen, nitrate, and particulate matter,
162 pH, $p\text{CO}_2$, chlorophyll fluorescence, zooplankton abundance and vertical migration (Lalande et
163 al., 2021, 2020), the presence of Arctic cod and zooplankton (Gonzalez et al., 2021), and the
164 vocalizations of marine mammals. During some years, the observatory included a third mooring,
165 an experimental “freeze-up detection mooring”, which transmitted real-time data of conductivity
166 and temperature throughout the water column until sea ice formation. The primary moorings
167 stretch from the seafloor at 46 m to about 33 m depth, designed to avoid collisions with ice keels.
168 Pressure sensors at the top of the moorings show less than ± 1 m of excursion of the moored
169 sensor package from its deployment mean depth in any given year, indicating that mooring blow-
170 over or diving is not the cause of any observed large variability. Description of the CEO and lists
171 of sensors deployed at the site can be found in Danielson et al. (2017) and Hauri et al., (2018).
172 For this study we focus on the inorganic carbon system and its controlling mechanisms.

173

174 **2.2 $p\text{CO}_2$**

175 We used a CONTROS HydroC CO_2 sensor (4H-Jena Engineering GmbH, Kiel, Germany) to
176 measure $p\text{CO}_2$. The Contros HydroC CO_2 sensor was outfitted with a pump (SBE 5M, Sea-Bird
177 Electronics) that flushes ambient seawater against a thin semi permeable membrane, which
178 serves as equilibrators for dissolved CO_2 between the ambient seawater and the headspace of the

179 sensor. Technical details about the sensor and its performance are described in Fietzek et al.
180 (2014), who estimated sensor accuracy to be better than 1% with postprocessing.

181 A HydroC CO₂ sensor has been deployed at the CEO site since 2016. In all deployments,
182 except 2016, HydroC CO₂ sensors were post-calibrated. The lack of post-calibration in 2016 is
183 not expected to negatively affect data quality because a battery failure resulted in data returns
184 only over the first 3 months (August through November). Following a zero interval where the
185 gas was pumped through a soda lime cartridge to create a zero-signal reference with respect to
186 CO₂, and subsequent flush interval to allow CO₂ concentrations to return to ambient conditions,
187 measurements were taken in a burst fashion every 12 or 24 hours depending on deployment year
188 (Table 1). Average *p*CO₂ values are reported as the mean of the measure interval (Table 1) with
189 standard uncertainty (Equation 1) defined following best practices (Orr et al., 2018) and where
190 the random component is the standard deviation of the mean, and the systematic components
191 include sensor accuracy and estimated error of the regression during calibration.

$$192 \quad u = \sqrt{u_{\text{systematic}}^2 + u_{\text{random}}^2} \quad (1)$$

193 More than 96% of the time, the relative uncertainty of the *p*CO₂ data met the weather data
194 quality goal, defined as 2.5% by the Global Ocean Acidification Observing Network (GOA-ON,
195 Newton et al., 2015).

196 HydroC CO₂ data were processed using Jupyter notebook scripts developed by 4H-Jena
197 Engineering GmbH using pre- and post-calibration coefficients interpolated with any change in
198 the zero-signal reference over the deployment (Fietzek et al., 2014). Further processing using in-
199 house MATLAB scripts included removal of outliers, calculation of the average *p*CO₂, and
200 calculation of uncertainty estimates for each measure interval.

201

202 **2.3 pH**

203 A SeapHOx sensor (Satlantic SeaFET™ V1 pH sensor integrated with Sea-Bird Electronics
204 SBE 37-SMP-ODO) was used to concurrently measure pH, salinity, temperature, pressure, and
205 oxygen (Martz et al., 2010). A SeapHOx was deployed at CEO in 2016, 2017, and 2018. No
206 SeapHOx was deployed in 2019 or 2020 due to supply chain delays and communication issues at
207 sea. Unfortunately, measured pH ($\text{pH}_{\text{SeaFET}}$) from the 2016 and 2018 SeapHOx deployments
208 were unusable due to high levels of noise in both the internal and external electrodes. In short,
209 we only have usable pH data between August 2017 and August 2018.

210 $\text{pH}_{\text{SeaFET}}$ data were excluded during a 14-day conditioning period following deployment and
211 were processed with post-calibration corrected temperature and salinity from the SBE37
212 following Bresnahan et al. (2014) using voltage from the external electrode (V_{ext}), and $\text{pH}_{V_{\text{ext}}}$
213 (pH calculated from the external electrode of the SeaFET) from an extended period of low
214 variability (18 February 2018). Despite the availability of discrete data from one calibration cast
215 (Cross et al., 2020b; Table 2), $\text{pH}_{V_{\text{ext}}}$ was used as the single calibration point (Bresnahan et al.,
216 2014) for a variety of reasons: 1) high variability of $\text{pH}_{\text{SeaFET}}$ (0.0581 pH units) straddling a 12
217 hour window around the discrete sample collection time, 2) high temporal and spatial variability
218 often seen in the Chukchi Sea, and 3) the discrete pH sample was within the published SeaFET
219 accuracy of 0.05 (Table 2, Figure S1). $\text{pH}_{\text{SeaFET}}$ values are reported as the mean of the measure
220 interval (Table 1) and standard uncertainty is calculated with Equation 1 with the standard
221 deviation of the average (random), and the SeaFET accuracy (systematic). Data handling and
222 processing were done using in-house MATLAB scripts. pH is reported in total scale and at *in*
223 *situ* temperature and depth for the entirety of this paper.

224

225 **2.4 Nitrate**

226 NO₃ measurements were from a Submersible Ultraviolet Nitrate Analyzer (SUNA) V2 by
227 Sea-Bird Scientific. The SUNA is an *in situ* ultraviolet spectrophotometer designed to measure
228 the concentration of nitrate ions in water. SUNA V2 data were processed using a publicly
229 available toolbox (Hennon et al., 2022; Irving, 2021) with QA/QC steps that included thermal
230 and salinity corrections (Sakamoto et al., 2009), assessment of spectra and outlier removal based
231 on spectral counts (Mordy et al., 2020), and concentration adjustments (absolute offset and linear
232 drift) based on pre-deployment and post-recovery reference measurements of zero concentration
233 (DI) water and a nitrate standard and, when available, nutrient samples taken from Niskin bottles
234 near the mooring site (e.g. Daniel et al., 2020).

235

236 **2.5 CTD and Oxygen**

237 Two CTDs were deployed on the CEO mooring near the HydroC CO₂ depth. The main
238 pumped Sea-Bird SeaCAT (SBE16) has been deployed on the CEO mooring around 33 m depth
239 since 2014. A pumped SBE43 oxygen sensor was deployed with the SBE16 during the 2015-
240 2016, 2017-2018, and 2019-2020 deployments but only data returns from the 2017-2018
241 deployment is discussed briefly in this manuscript (Figure S2).

242 The other pumped CTD was a Sea-Bird MicroCAT (SBE37-SMP-ODO), which was
243 integrated with an optical dissolved oxygen sensor (SBE63; Figure S2), and the SeaFET pH
244 sensor within the SeapHOx instrument. The SeapHOx was deployed in fall 2016, 2017, and
245 2018. The SBE37-SMP-ODO did not record any CTD or oxygen data during the 2016
246 deployment and only recorded CTD and oxygen data between August and November 3 in 2018
247 due to battery failure.

248 Processing of these data included temperature and conductivity correction using pre- and
249 post-calibration data following Sea-Bird Application Note 31 and oxygen correction using pre-
250 and post-calibration data following Sea-Bird Module 28. Oxygen was converted from ml/l to
251 $\mu\text{mol/kg}$ following Bittig et al. (2018). Density and practical salinity were calculated using the
252 TEOS-10 GSW Oceanographic Toolbox (McDougall and Baker, 2011).

253 Differences between the two oxygen sensors (SBE43 and SBE63) of approximately 145 to
254 265 $\mu\text{mol/kg}$ were observed over the 2017-2018 deployment, and both moored sensors had
255 varying offsets compared to nearby casts (Figure S2). Therefore, only relative oxygen values
256 from the freshly calibrated SBE63 are discussed in this paper.

257 The freeze-up detection mooring (Figure 6) consisted of four Sea-Bird SBE 37 inductive
258 modem CTD sensors that transmitted in real time hourly temperature, salinity, and pressure data
259 via the surface float from four subsurface depths (8, 20, 30, and 40 m; Hauri et al., 2018).

260

261 **2.6 Development of empirical relationship to estimate pH**

262 Empirical relationships for estimating water column pH have been developed for regions
263 spanning southern, tropical, temperate and Arctic biomes, using a variety of commonly measured
264 parameters (e.g., $\text{pH}(\text{S}, \text{T}, \text{NO}_3, \text{O}_2, \text{Si})$ Carter et al 2018; $\text{pH}(\text{O}_2, \text{T}, \text{S})$ Li et al., 2016; $\text{pH}(\theta, \text{O}_2)$
265 Watanabe et al., 2020; $\text{pH}(\text{NO}_3, \text{T}, \text{S}, \text{P})$ and $\text{pH}(\text{O}_2, \text{T}, \text{S}, \text{P})$ Williams et al., 2016; $\text{pH}(\text{O}_2, \text{T})$
266 Alin et al., 2012; $\text{pH}(\text{O}_2, \text{T})$ and $\text{pH}(\text{NO}_3, \text{T})$ Juranek et al., 2009). Given the tight coupling
267 between the concentration of H^+ and concentration of CO_2 solution, an empirical relationship for
268 estimating surface pH from $p\text{CO}_2$ was developed by the National Academies of Sciences,
269 Engineering and Medicine (2017) appendix F. Licker et al. (2019) used this empirical
270 relationship to calculate the global average surface ocean pH and found it represented the

271 relationship for surface water temperatures spanning 5°C to 45°C. Here, we take a similar
272 approach but extend it to water column pH in our cold region using temperature (T) and salinity
273 (S) as additional proxy parameters (Equation 2).

$$274 \quad pH^{est} = \alpha_0 + \alpha_1 \log(pCO_2) + \alpha_2 T + \alpha_3 S \quad (2)$$

275 Where pH^{est} is the estimated value of water column pH, pCO_2 is from the HydroC, and T and S
276 are from the SBE16, and all α ($\alpha_0 = 10.4660$, $\alpha_1 = -0.4088$, $\alpha_2 = 0.0013$, $\alpha_3 = -0.0001$) terms are
277 model-estimated coefficients determined using MATLAB's multiple linear regression algorithm
278 *regress.m* (Chatterjee and Hadi, 1986). After interpolating pH_{SeaFET} (Figure 4, red dots) to the
279 pCO_2 timestamp, the algorithm was trained over an arbitrarily chosen 180-day period
280 (15/9/2017-14/3/2018, Figure 4, dashed box). An uncertainty of 0.0525 for pH^{est} (Figure 3 and
281 Figure S1, gray shading) was determined with Equation 1, where the RMSE (the uncertainty in
282 the estimation) over the entire pH_{SeaFET} timeseries is the random component and the published
283 accuracy of the SeaFET is the systematic component (since the algorithm was trained with
284 pH_{SeaFET}). The algorithm cross-validation and evaluation are discussed in section 3.1. Unless
285 explicitly defined otherwise, observations of pH refer to pH^{est} for the remainder of this paper.

286

287 **2.7 Carbonate system calculations**

288 Moored data were collected at different sample intervals (Table 1) and were linearly
289 interpolated to the HydroC CO_2 timestamp to enable further calculations. TA, DIC, and Ω_{arag}
290 (Figure 11 a & b and Figure 3d) were calculated based on measured pCO_2 , S, T, and pressure (P)
291 and algorithm-based pH (pH^{est}). Due to a lack of data, nutrient concentrations (Si, PO_4 , NH_4 ,
292 H_2S) were assumed to be negligible in the CO2SYS calculations (e.g. deGrandpre et al., 2019;
293 Vergara-Jara et al., 2019; Islam et al., 2017). pH^{est} was used in lieu of pH_{SeaFET} to allow for

294 calculations over the whole $p\text{CO}_2$ record and due to erroneously large variability of DIC and TA
295 when $\text{pH}_{\text{SeaFET}}$ was used as an input parameter (Raimondi et al., 2019; Cullison-Gray et al.,
296 2011). The pH - $p\text{CO}_2$ input pair leads to large, calculated errors in DIC and TA (Raimondi et al.,
297 2019; Cullison-Gray et al., 2011) due to strong covariance between the two parameters (both
298 temperature and pressure dependent). Cullison-Gray et al. (2011) attributed unreasonably large
299 short-term variability in calculated TA and DIC to temporal or spatial measurement mismatches
300 between input pH and $p\text{CO}_2$ parameters and found that appropriate filtering alleviated noise
301 spikes. By using pH^{est} , which by the nature of its definition is well correlated to $p\text{CO}_2$, we are
302 eliminating some of these spurious noise spikes. We show Ω_{arag} calculated from $\text{pH}_{\text{SeaFET}}-p\text{CO}_2$
303 (Figure 3d, red line) because it is less sensitive to calculated errors as it accounts for a small
304 portion of the total CO_2 in seawater (Cullison-Gray et al., 2011).

305 All inorganic carbon parameters were calculated using CO2SYSv3 (Sharp et al., 2023; Lewis
306 and Wallace, 1998) with dissociation constants for carbonic acid of Lueker et al. (2000),
307 bisulfate of Dickson (1990), hydrofluoric acid of Perez and Fraga (1987), and the boron-to-
308 chlorinity ratio of Lee et al. (2010). Sulpis et al. (2020) found that the carbonic acid dissociation
309 constants of Lueker et al. (2000) may underestimate $p\text{CO}_2$ in cold regions (below $\sim 8^\circ\text{C}$), and
310 therefore overestimate pH and CO_3^{2-} . However, we choose to use Lueker et al. (2000) because
311 they are recommended (Dickson et al., 2007; Woosley, 2021), continue to be the standard (Jiang
312 et al., 2021; Lauvset et al., 2021), and are commonly used at high latitudes (Duke et al., 2021;
313 Raimondi et al., 2019; Woosley et al., 2017). Furthermore, the difference between DIC
314 calculated from pH^{est} and $p\text{CO}_2$ and discrete samples interpolated to moored instrument depth
315 ranged from 266 to $-195 \mu\text{mol}/\text{kg}$ using the K_1^* and K_2^* of Sulpis et al. (2020), compared to -38
316 to $-7 \mu\text{mol}/\text{kg}$ using Lueker et al. (2000).

Deleted: k

Deleted: k

Formatted: Superscript

Formatted: Superscript

319

320 **2.8 Sea ice concentration**

321 Sea ice concentration at the observatory site was taken from the National Snow and Ice Data
322 Center (NSIDC; DiGirolamo et al., 2022). Latitude and longitude coordinates were converted to
323 NSIDC's EASE grid coordinate system (Brodzik and Knowles, 2002) and the 25-km gridded
324 data were bilinearly interpolated to calculate sea ice concentration at the CEO site. Low sea ice is
325 defined by < 15 % sea ice coverage per grid cell.

326

327 **2.9 Estimation of model-based ocean acidification trend**

328 Model results were obtained from historical simulations of five different global Earth System
329 Models: 1) GFDL-CM4 (Silvers et al., 2018), 2) GFDL-ESM4 (Horowitz et al., 2018), 3) IPSL-
330 CM6A-LR-INCA (Boucher et al., 2020), 4) CNRM-ESM2-1 (Seferian, 2019), and 5) Max Plank
331 Earth System Model 1.2 (MPI-ESM1-2-LR, Wieners et al., 2019) that are part of the Coupled
332 Model Intercomparison Project Phase 6 (CMIP6). Each simulation was used to calculate the
333 annual trend of aragonite saturation state and pH at the closest depth and grid cell to the CEO
334 mooring.

335

336 **3. Results**

337 In the following, we will evaluate the pH algorithm (section 3.1), analyze the large
338 variability patterns (sections 3.2 and 3.3), and then take a closer look at the data from 2020 since
339 the seasonal cycle was different in 2020 than in previous years (section 3.4).

340

341 **3.1 pH algorithm**

342 The algorithm estimated pH data from the CEO site reasonably well and within the weather
343 uncertainty goal as defined by Newton et al. (2015) most of the time. As a first step, pH^{est}
344 consistency was assessed through cross-validation (Figure 5) using the test dataset (outside the
345 training period, $r^2 = 0.9666$, $\text{RMSE} = 0.166$) and across the whole timeseries ($r^2 = 0.9598$, RMSE
346 $= 0.0161$, $p < 0.0001$, Figure 5). Observed high frequency spikes in $\text{pH}_{\text{SeaFET}}$ (Figure 4, red dots;
347 Figure 5d, red line) were not captured by the HydroC $p\text{CO}_2$ sensor (sampling frequency of 12 h)
348 and as a result, are not reproduced in the pH^{est} timeseries. Throughout the $\text{pH}_{\text{SeaFET}}$ timeseries,
349 pH^{est} overestimates $\text{pH}_{\text{SeaFET}}$ by a mean of 0.0008 and median of 0.0039. Since pH^{est} generally
350 overestimates $\text{pH}_{\text{SeaFET}}$, we assume that Ω_{arag} is also somewhat overestimated throughout this
351 manuscript. Discrete water samples were used as reference values to evaluate the algorithm at
352 the CEO site (Table 2) and were found to be within the pH^{est} uncertainty (Figure S1).

353 An independent verification of our algorithm was done using discrete data collected from the
354 Bering Sea to the Arctic Ocean on four research cruises in 2020, 2019, 2018, and 2017 (Figure
355 6d; Monacci et al., 2022; Cross et al., 2021; 2020a; 2020b), henceforth called the DBO dataset.
356 Samples collected from deeper than 500 m below the surface or flagged as questionable or bad
357 were excluded from this analysis. pH and $p\text{CO}_2$ were calculated from 1275 discrete samples
358 analyzed for TA, DIC, silicate, phosphate, and ammonium (except when silicate, phosphate, and
359 ammonium were assumed to be negligible for the 327 samples from [cruise SKQ202014S](#);
360 Monacci et al., 2022) using CO2SYSv3 (Sharp et al., 2023; section 2.7 for details) and are
361 referred to as $\text{pH}^{\text{disc}}_{\text{calc}}$ and $p\text{CO}_2^{\text{disc}}_{\text{calc}}$, respectively. $\text{pH}^{\text{disc}}_{\text{est}}$ was based on discrete water samples
362 and calculated using Equation 2 and was fit to $\text{pH}^{\text{disc}}_{\text{calc}}$ using a linear regression ($r^2 = 0.9975$,
363 $\text{RMSE} = 0.0078$, $p\text{-value} < 0.0001$; Figure 6 a – c). Mean and median differences between
364 $\text{pH}^{\text{disc}}_{\text{calc}}$ and $\text{pH}^{\text{disc}}_{\text{est}}$ were zero and 0.0022, respectively, with largest anomalies observed at

Deleted: (mean difference of 0.0008)

366 lower salinities (Figure 6c). Absolute differences between $\text{pH}^{\text{disc}}_{\text{est}}$ and $\text{pH}^{\text{disc}}_{\text{cal}}$ over the salinity
367 range observed at the CEO site (30.87 to 33.93) fall within the weather data quality goal
368 (Newton et al., 2015) 98.7% of the time with maximum absolute differences < 0.03 . The
369 uncertainty of 0.0154 for $\text{pH}^{\text{disc}}_{\text{est}}$ was determined using Equation 1, where the mean combined
370 standard uncertainty (u_c) for $\text{pH}^{\text{disc}}_{\text{calc}}$ (0.0133; Orr et al., 2018) was the systematic component,
371 and the regression RMSE was the random component.

372 Empirical relationships for estimating water column pH that rely on dissolved oxygen often
373 ignore surface waters to limit biases due to decoupling the stoichiometry of the $\text{O}_2:\text{CO}_2$
374 relationship due to air-sea gas exchange (e.g. Juranek et al., 2011; Alin et al., 2012; Li et al.,
375 2016). We see evidence of this bias in our algorithm at low salinity (Figure 6c) and low $p\text{CO}_2$
376 (not shown) when compared with the DBO dataset samples collected across the Arctic and from
377 the surface to 500 m, with $\text{pH}^{\text{disc}}_{\text{est}}$ overestimating $\text{pH}^{\text{disc}}_{\text{calc}}$ by a maximum of 0.049. If depth is
378 restricted to between 30 and 500 m when evaluating the algorithm with the DBO dataset,
379 algorithm performance improves ($r^2 = 0.9990$, $\text{RMSE} = 0.0055$, $p\text{-value} < 0.0001$; not shown)
380 and the maximum $\text{pH}^{\text{disc}}_{\text{est}}$ overestimates $\text{pH}^{\text{disc}}_{\text{calc}}$ by 0.022.

381

382 3.2 Relaxation events

383 The sub-surface waters at the CEO site comprise a high $p\text{CO}_2$, low pH, and low Ω_{arag}
384 environment, with mean values of $p\text{CO}_2^{\text{mean}} = 538 \pm 7 \mu\text{atm}$, $\text{pH}^{\text{mean}} = 7.91 \pm 0.05$, $\Omega_{\text{arag}}^{\text{mean}} =$
385 0.94 ± 0.23 across the full data record (Figure 3 b - d). In the following we will focus on spikes
386 of high pH and Ω_{arag} and low $p\text{CO}_2$ that occur in spring (May-June) and fall (September-
387 December); we define these spikes as relaxation events (see discussion for justification of term).

388 Spring: Springtime relaxation events at 33 m depth that exhibit relatively higher pH and
389 Ω_{arag} and lower $p\text{CO}_2$ compared to the overall mean, are likely consequences of photosynthetic
390 activity during sea ice break-up (Figures 2 and 3). In June of ~~2018 and 2019~~, near bottom pH and
391 Ω_{arag} spiked to > 8.17 and > 1.5 , respectively, while $p\text{CO}_2$ dropped to $< 286 \mu\text{atm}$. Ω_{arag} remained
392 oversaturated and pH was greater than 8.0 for nearly all of June in 2018. In 2019, the relaxation
393 event was less sustained, with only four short (2-6 day-long) events of relatively higher pH and
394 $\Omega_{\text{arag}} > 1$ in June. In both years, chlorophyll fluorescence spiked and either O_2 increased (in
395 2018) or NO_3 decreased (in 2019), which are signs of photosynthetic activity and primary
396 production.

397 Fall: The relaxation events in fall were characterized by large and sudden drops in $p\text{CO}_2$,
398 abrupt increases in pH and Ω_{arag} , and considerable interannual variability in their timing. Unlike
399 the relaxation events observed in spring, we attribute these fall relaxation events to wind-induced
400 physical mixing. To examine the controlling mechanisms causing these abrupt relaxation events
401 in fall, we will start with using water column salinity and temperature data from a freeze-up
402 detection buoy (Hauri et al., 2018) that was deployed in summer 2017 approximately 1 km away
403 from the biogeochemical mooring. The freeze-up detection mooring provided temperature and
404 salinity measurements every 7 meters throughout the water column from the time of its
405 deployment in mid-August until freeze-up. Data from the freeze-up detection mooring suggest
406 that warmer and fresher water from the upper water column gets periodically entrained down to
407 the location of the biogeochemical sensor package at 33 m depth, leading to enhanced variability
408 of density in August and September (Figure 7). Fluctuations of the pycnocline associated with
409 the passage of internal waves could also elevate signal variances. During this time $p\text{CO}_2$ often
410 decreased to or below atmospheric levels and pH sporadically reached values > 8 . At the end of

Deleted: 2019

Deleted: 2020

413 September, a strong mixing event (with coincident strong surface winds) homogenized the water
414 column from the surface down to the location of the sensor package and caused a sudden
415 temperature increase from 0.4 °C to 3.9 °C (Figure 7c and 8a). At the same time, $p\text{CO}_2$ (Figure
416 7b and 8) decreased from 590 to 308 μatm . This suggests that warm and low CO_2 surface water
417 mixed with CO_2 -rich subsurface water and led to a sustained relaxation period that subsequently
418 lasted until mid-November. Another mixing event further eroded the water column stratification
419 and replaced subsurface water with colder and fresher water (ice melt) from the surface at the
420 end of October. This second large mixing event did not lead to large changes in $p\text{CO}_2$, pH, and
421 Ω_{arag} .

422 Salinity and temperature records from the biogeochemical mooring at 33 m depth also
423 suggest fall season mixing events in all other years, when increases in temperature coincide with
424 decreases in $p\text{CO}_2$ (Figure 2b and c, 3a and 8). For example, two mixing events shaped the
425 carbonate chemistry evolution in fall 2018. $p\text{CO}_2$ decreased from 915 μatm to around 565 μatm
426 and Ω_{arag} increased to 0.9 as temperature increased and salinity decreased in early September
427 (Figures 2 and 8). $p\text{CO}_2$ then increased to 1160 μatm in late October, before decreasing to 385
428 μatm at the beginning of November, causing a spike in Ω_{arag} to 1.34. At the same time, salinity
429 decreased by 1 unit, suggesting a strong mixing event. Throughout November 2018, $p\text{CO}_2$
430 oscillated between 344 and 757 μatm and salinity between 31.01 and 32.97, hinting at additional
431 mixing.

432 Similarly, an early mixing event in 2019 decreased $p\text{CO}_2$ to 352 μatm at the beginning of
433 September. Short-term variability in $p\text{CO}_2$ with maximum levels of up to 855 μatm and
434 minimum values below 300 μatm , variable temperature and salinity, and sporadic aragonite
435 oversaturation events point to mixing through mid-September. At the end of October, a large

436 mixing event homogenized the water column, accompanied by a decline of salinity by >1 unit,
437 increase of temperature to 4 °C, and decrease of $p\text{CO}_2$ from 565 μatm to below 400 μatm . In a
438 similar fashion to 2018, this fall mixing event was followed by a month-long period of large
439 variability of $p\text{CO}_2$, salinity, pH, and Ω_{arag} , leading to short and sporadic aragonite oversaturation
440 events in November, and sustained oversaturation in December.

441

442 3.3 Sustained periods of low pH and Ω_{arag} , and high $p\text{CO}_2$

443 Waters at 33 m depth at the CEO site were most acidified during the sea ice free periods
444 until mixing events entrained surface waters to the sensor depth (section 3.2). pH and Ω_{arag}
445 started to gradually decrease from their maximum levels ($\Omega_{\text{arag_max}} = 1.65$, $\text{pH}_{\text{max}} = 8.19$) at the
446 beginning of June in 2018 to their annual low at the beginning of November ($\Omega_{\text{arag_min}} = 0.47$,
447 $\text{pH}_{\text{min}} = 7.58$, Figure 3 d and e). In November, the waters were also undersaturated with regards
448 to calcite (not shown) and $p\text{CO}_2$ peaked at 1159 μatm (Figure 3b). Dissolved oxygen decreased
449 by about 400 $\mu\text{mol kg}^{-1}$ between July and October, when the sensor stopped working properly.
450 The decrease of dissolved oxygen suggests remineralization of organic material. The decrease of
451 pH, Ω_{arag} , O_2 and increase of $p\text{CO}_2$ was briefly interrupted by a strong mixing event in
452 September, which entrained warmer, fresher, and CO_2 -poorer water down to 33 m depth (section
453 3.2, Figure 8). The 2019 observations paint a similar picture of remineralization during the
454 summer months, as the $p\text{CO}_2$ increase and pH and Ω_{arag} decreases were accompanied by an NO_3
455 increase (Figure 2d and 3b-d).

456 $p\text{CO}_2$ steadily increased and pH and Ω_{arag} decreased during the sea ice covered periods
457 (Figures 8). pH was < 8 and Ω_{arag} remained undersaturated under the sea ice. At the same time,
458 NO_3 slowly increased and O_2 decreased, which points to slow organic matter remineralization

459 (Figure 9). Short-term variability in $p\text{CO}_2$, especially in January of all three observed years, was
460 also reflected in salinity, O_2 and NO_3 (Figure 9) and could be attributed to advection, as the CEO
461 site is adjacent to contrasting regimes of flow and hydrographic properties (Fang et al., 2020).

462

463 **3.4 Spring and summer of 2020 were different**

464 The seasonal cycle in 2020 strongly contrasted with the previous observed years. $p\text{CO}_2$
465 gradually increased by roughly 200 μatm throughout the sea ice covered months to 650 μatm
466 when sea ice started to retreat at the beginning of July. By the end of July, $p\text{CO}_2$ doubled and
467 increased to 1389 μatm , which is the highest $p\text{CO}_2$ level recorded in this timeseries. The peak of
468 $p\text{CO}_2$ was accompanied by an increase in salinity of 0.5 while temperature did not change,
469 suggesting the influence of advection. At the beginning of August, $p\text{CO}_2$ dropped to 536 μatm
470 and then oscillated around 600 μatm through much of August before returning to around 900
471 μatm for the next month. Similarly, pH decreased to 7.5 at the end of July and then oscillated
472 around 7.85, while Ω_{arag} dropped to 0.37, and oscillated around 0.85. The steep drop and
473 oscillation of $p\text{CO}_2$ was reflected in NO_3 , suggesting that primary production and
474 remineralization played a role. When $p\text{CO}_2$ and NO_3 decreased at the beginning of August,
475 temperature simultaneously increased by 0.7 $^\circ\text{C}$ and salinity decreased by 0.12, suggesting that
476 entrainment of shallower water masses may have played a role too. Comprehensive analyses of
477 the factors that resulted in the 2020 differing conditions are beyond the scope of this paper, but
478 deserve attention in a future effort.

479

480 **4. Discussion**

481 CEO data provide new insights into the synoptic, seasonal and interannual variability of
482 the inorganic carbon system in a time when ocean acidification and climate change have already
483 started to transform this area. The observations suggest that the CEO site is a high-CO₂ and low-
484 pH and low- Ω_{arag} environment most of the time, except during sea ice break-up when the effects
485 of photosynthetic activity remove CO₂ from the system, and later in fall, when strong storm
486 events entrain low $p\text{CO}_2$ surface waters to the seafloor. Lowest pH and CaCO₃ saturation states
487 and highest $p\text{CO}_2$ occur in summer through late fall when organic matter remineralization
488 dominates the carbonate system balance. During this time, Ω_{arag} can fall below 0.5 and even Ω_{calc}
489 becomes sporadically undersaturated ($\Omega_{\text{calc}} < 1$).

490

491 **4.1 pH algorithm**

492 Deploying oceanographic equipment in remote Arctic locations is challenging. The data
493 return from the SeapHOx sensors was disappointingly minimal, despite annual servicing and
494 calibration by the manufacturer. Our new pH algorithm is therefore even more important as it
495 fills pH data gaps in the CEO timeseries and can be applied with confidence from the Bering to
496 the [western](#) Beaufort seas (Figure 6). While another successful year of moored pH data return at
497 the CEO site is needed to fully evaluate our algorithm throughout the year, comparison with
498 single discrete water samples nearby the CEO site and the DBO dataset (section 3.1, Table 2,
499 Figures 6 and S1) suggest that our algorithm-derived pH meets the weather quality uncertainty
500 goal of ± 0.02 (Newton et al., 2015) much of the time.

501 The combination of our new algorithm with recent progress in monitoring $p\text{CO}_2$ with
502 Seagliders (Hayes et al., 2022) will further increase our ability to study the inorganic carbon
503 dynamics at times and locations when shipboard or mooring based measurements may not be

504 practical. Additional assessment is needed to determine to what degree the algorithm needs
505 adjustments beyond the region evaluated in this work.

506

507 **4.2 Uncertainty**

508 Inherent spatial and temporal variability of the inorganic carbon parameters in the
509 Chukchi Sea make the use of discrete water samples for evaluating sensor-based measurements
510 difficult. Historic continuous surface measurements from the area suggest that surface $p\text{CO}_2$ can
511 be as low $< 250 \mu\text{atm}$ in early fall (Hauri et al., 2013), at a time of year when subsurface $p\text{CO}_2$
512 reaches its max of $> 800 \mu\text{atm}$ at the CEO site. This suggests a steep $p\text{CO}_2$ gradient of $> 17 \mu\text{atm}$
513 per meter. High-resolution pH data from the 2017/2018 deployment suggests high temporal
514 variability as well, further complicating the collection of discrete water samples to adequately
515 evaluate the sensors. The HydroC's zeroing function, in addition to our pre- and post-calibration
516 routines that factor into the post-processing of the data, gives us confidence in the accuracy of
517 the $p\text{CO}_2$ data, and further confidence in pH derived from $p\text{CO}_2$.

518 The pH^{est} uncertainty of 0.0525 is likely a conservative estimate based on our validation
519 of pH^{est} (section 3.1, Table 2). Consequently, propagated uncertainties in the calculated
520 parameters are high. As discussed in section 2.7, the pH- $p\text{CO}_2$ input pair exacerbates these larger
521 uncertainties. Mean $\text{TA}(\text{pH}^{\text{est}}, p\text{CO}_2)$, $\text{DIC}(\text{pH}^{\text{est}}, p\text{CO}_2)$, and $\Omega_{\text{arag}}(\text{pH}^{\text{est}}, p\text{CO}_2)$, $\pm u_c$ (Orr et al.,
522 2018) are $2173 \pm 281 \mu\text{mol kg}^{-1}$, $2111 \pm 263 \mu\text{mol kg}^{-1}$, and 0.94 ± 0.23 , respectively, when
523 input uncertainties are the standard uncertainty (Equation 1). When the input uncertainty for
524 pH^{est} is only the RMSE of 0.0161 (section 3.1), uncertainties decrease to $\pm 98 \mu\text{mol kg}^{-1}$, ± 93
525 $\mu\text{mol kg}^{-1}$, and ± 0.09 , respectively. When input uncertainties are only the random component of
526 the input parameters (i.e. standard deviation for $\text{pH}_{\text{SeaFET}}$ and $p\text{CO}_2$ and instrument precision for

527 T and S), $TA(pH_{\text{SeaFET}}, pCO_2)$, $DIC(pH_{\text{SeaFET}}, pCO_2)$, and $\Omega_{\text{arag}}(pH_{\text{SeaFET}}, pCO_2)$ u_c drops to ± 38
528 $\mu\text{mol kg}^{-1}$, $\pm 37 \mu\text{mol kg}^{-1}$, and ± 0.06 , respectively. Given the above uncertainties and that we
529 do not see significant biofouling at the CEO site, we believe that short term variability can be
530 discussed with confidence with this dataset. In other words, wiggles in the data represent real
531 events, despite the high uncertainty in the precise value of the calculated parameters.

532

533 4.3 Subsurface biogeochemical drivers of pH, Ω_{arag} , and pCO_2

534 Inorganic carbon chemistry can be influenced by advection and vertical entrainment of
535 different water masses, temperature, salinity, biogeochemistry, and conservative mixing with TA
536 and DIC freshwater endmembers. Here, we followed Rheuban et al. (2019) and separated the
537 drivers of the observed large pH, Ω_{arag} , and pCO_2 variability to provide additional insights into
538 our timeseries (Figure 10) using CO2SYS by altering input parameters temperature, salinity, TA,
539 and DIC. Anomalies (black) relative to the reference values $pH(T_0, S_0, DIC_0, TA_0)$, $\Omega_{\text{arag}}(T_0, S_0,$
540 $DIC_0, TA_0)$, and $pCO_2(T_0, S_0, DIC_0, TA_0)$, were calculated using a linear Taylor series
541 decomposition, adding up the thermodynamic effects of temperature and salinity, and the
542 perturbations due to biogeochemistry, and conservative mixing with freshwater DIC and TA
543 endmembers (Rheuban et al., 2019). Reference values $T_0, S_0, DIC_0,$ and $TA_0,$ are the mean of the
544 CEO timeseries. Freshwater from sea ice melt and meteoric sources (precipitation and rivers)
545 may influence the CEO site. TA and DIC concentrations of $450 \mu\text{mol kg}^{-1}$ and $400 \mu\text{mol kg}^{-1}$,
546 respectively, have been measured in Arctic sea ice (Rysgaard et al., 2007). Riverine input along
547 the Gulf of Alaska tends to have lower TA ($366 \mu\text{mol kg}^{-1}$) and DIC ($397 \mu\text{mol kg}^{-1}$)
548 concentrations (Stackpoole et al., 2016, 2017) than rivers draining into the Bering, Chukchi, and
549 Beaufort Seas (TA = $1860 \mu\text{mol kg}^{-1}$, DIC = $2010 \mu\text{mol kg}^{-1}$, Holmes et al., 2021) all of which

Deleted: .

551 can influence the CEO site to some extent (Asahara et al., 2012; Jung et al., 2021). In this Taylor
552 decomposition we used sea ice TA and DIC endmembers (Rysgaard et al., 2007) but want to
553 emphasize that using Arctic river endmembers did not meaningfully change the results (not
554 shown). Figure 10 shows the effects of biogeochemical processes, temperature, salinity, and
555 conservative mixing with TA and DIC freshwater endmembers on pH, Ω_{arag} , and $p\text{CO}_2$. The
556 effects of salinity (turquoise) and conservative mixing with TA and DIC freshwater endmembers
557 (green) are negligible for pH, Ω_{arag} , and $p\text{CO}_2$. Temperature varied between -1.7 °C during the
558 sea ice covered months and up to 4 °C in late fall, when wind events mixed the whole water
559 column and entrained warm and low $p\text{CO}_2$ surface waters to the instrument depth at 33 m (see
560 section 3.2 for a more in-depth discussion of these mixing events). During this time, the increase
561 in temperature counteracted the effect of biogeochemistry slightly and increased $p\text{CO}_2$ and
562 decreased pH (Figure 10 a,c). Temperature did not affect Ω_{arag} .

563 Biogeochemistry (photosynthesis, respiration, calcification, dissolution) is the most
564 important driver of the inorganic carbon dynamics at 33 m depth at the CEO site. The springtime
565 relaxation events in 2018 and 2019 with relatively higher pH and Ω_{arag} , and lower $p\text{CO}_2$, were
566 mainly driven by biogeochemistry (Figure 10, magenta). During these events O_2 increased and
567 NO_3 decreased, suggesting photosynthetic activity (Figure 2d, e and 3a). Near bottom
568 photosynthetic activity by phytoplankton or sea ice algae has been observed at different locations
569 across the Chukchi Sea (Arrigo et al., 2017; Ouyang et al., 2022; Stabeno et al., 2020; Koch et
570 al., 2020). Sediment trap data from a CEO deployment prior to the start of this $p\text{CO}_2$ and pH
571 time-series suggest that export of the exclusively sympagic sea ice algae *Nitzschia frigida* peaked
572 in May and June, during snow and ice melt events (Lalande et al., 2020), further supporting the
573 hypothesis that sea ice algae contributed to the CO_2 draw down. Interestingly, TA also increased

Deleted: red

575 significantly during these events in 2018 and 2019, which cannot be solely attributed to organic
576 matter production. Specifically, TA increased by 23 $\mu\text{mol kg}^{-1}$ in 2019 (Figure 11a). However,
577 with an observed NO_3 decrease of 7.6 $\mu\text{mol kg}^{-1}$, we would expect an increase of TA by 7.6 μmol
578 kg^{-1} . This is assuming that NO_3 is the primary source of nitrogen during organic matter
579 formation, and that assimilation of 1 μmol of NO_3 leads to an increase of TA of 1 μmol (Wolf-
580 Gladrow et al., 2007). The TA increase of 23 $\mu\text{mol kg}^{-1}$ is therefore larger than expected from
581 organic matter formation alone and is likely due to CaCO_3 mineral dissolution. While direct
582 evidence is missing, the strong TA increase suggests that CaCO_3 mineral dissolution during sea
583 ice break up also plays an important role at the CEO site. As observed in other Arctic areas, it is
584 possible that ikaite crystals that were trapped in the ice matrix dissolved in the water column
585 when sea ice melted (Rysgaard et al., 2012, 2007).

586

587 4.4 Progression of ocean acidification in the Chukchi Sea

588 Organisms living at the CEO site may have always been exposed to large seasonal
589 variability and low pH and Ω_{arag} (high $p\text{CO}_2$), but the combined and cumulative effects of
590 climate change and ocean acidification have rapidly made these conditions more extreme and
591 longer lasting. Ocean acidification serves as a gradual environmental press by increasing the
592 system's mean and extreme $p\text{CO}_2$ and decreasing mean and extreme pH and Ω_{arag} . Climate
593 induced changes to other important controls of the inorganic carbon system, such as sea ice,
594 riverine input, temperature, and circulation can act as sudden pulses and further modulate the
595 inorganic carbon system to a less predictable degree and cause extreme events (Woosley and
596 Millero, 2020; Orr et al., 2022; Hauri et al., 2021; Qi et al., 2017). Huntington et al. (2020)
597 describe a sudden and dramatic shift of the physical, biogeochemical and ecosystem conditions

Deleted: increase

Formatted: Superscript

Deleted: The Arctic Ocean acidification rate will continue to exceed the rate of CO_2 change in the atmosphere because of the impacts of freshening and other more localized, seasonal or short-term consequences of climate change (Woosley and Millero, 2020; Terhaar et al., 2021; Orr et al., 2022; Qi et al., 2017). Seventeen years of ship-based data from sub surface Chukchi Summer water suggests a mean pH change of -0.0047 ± 0.0026 and mean Ω_{arag} change of -0.017 ± 0.009 (Qi et al., 2022b). As a comparison, an average across historic simulations from five CMIP6 models (see methods) estimates a change in pH of $-0.0077 \text{ year}^{-1}$ and Ω_{arag} of $-0.0063 \text{ year}^{-1}$ at 33 m of the CEO site between 2002 – 2014. The historic CMIP6 simulations end in 2014 and therefore miss the last years of extreme sea ice loss. Both observations and global model-based trend estimates must be used with caution. The observations were collected during the sea ice free period (Qi et al., 2022b), and therefore do not depict an annually representative trend. Global models do not resolve important local physical, chemical, and biological meso-scale processes and therefore mask out the variability of the inorganic carbon system and effects of climate change. ¶

620 in the Chukchi and Northern Bering seas in 2017. For example, satellite data for the CEO site
621 illustrate that the longest open water seasons on record occurred between 2017 and 2020. Before
622 2017, the open water season was on average $81 (\pm 40)$ days long (i.e., below 15 %
623 concentration), of which $60 (\pm 44)$ days were ice free, whereas between 2017 and 2020, the low
624 sea ice period was $157 (\pm 30)$ days long, of which $152 (\pm 24)$ days were ice free (Figure 12). Sea
625 ice decline and increased nutrient influx has also promoted increased phytoplankton primary
626 production in the area (Lewis et al., 2020; Arrigo and van Dijken, 2015; Payne et al., 2021).
627 Since our inorganic carbon timeseries started after the “dramatic shift” that was observed in the
628 Chukchi Sea in 2017 (Huntington et al., 2020) and given the uncertainty in model output in this
629 region, we can only speculate about how the changes in sea ice, temperature and biological
630 production may have affected seasonal variability and extremes of the inorganic carbon
631 chemistry at the CEO site. However, since the summertime low pH and Ω_{arag} and high $p\text{CO}_2$ are
632 tightly coupled to the length of the ice-free period and intensity of organic matter production, it
633 is possible that the observed summertime period of extreme conditions may have been
634 previously unexperienced at this site. We therefore think it is justified to call the spikes of pH
635 and Ω_{arag} “ocean acidification relaxation events”, since the long-lasting summertime period of
636 extremely low pH and Ω_{arag} may be a new pattern.

637

638 **4.5 Relevance for ecosystem**

639 Marine organisms are exposed to a wide range of naturally fluctuating environmental
640 conditions such as temperature, salinity, carbonate chemistry and food concentrations that
641 together constitute their ecological niche. As evolution works toward adaptation, the tolerance
642 range of species and ecosystems to such parameters varies between locations and is often closely

643 related to niche status (Vargas et al., 2022). Stress can be defined as a condition evoked in an
644 organism by one or more environmental and biological factors that bring the organism near or
645 over the limits of its ecological niche (after Van Straalen, 2003). The consequence of the
646 exposure to a stressor will depend on organismal sensitivity, stress intensity (how much it
647 deviates from present conditions) and stress duration. In a synthesis of the global literature on the
648 biological impacts of ocean acidification, Vargas et al. (2017, 2022) showed that the extreme of
649 the present range of variability of carbonate chemistry is a good predictor of species sensitivity.
650 In other words, larger deviations from present extreme high $p\text{CO}_2$ or extreme low pH, would be
651 expected to exert more negative biological impacts. Organismal stress and niche boundaries have
652 implications for the definition and understanding of controls and future ocean acidification
653 conditions in experiments aimed at evaluating future biological impacts.

654 Our data provide insights on conditions that affect and determine local species'
655 ecological niches, and a necessary key is to evaluate or re-evaluate their sensitivity to present and
656 future carbonate chemistry conditions, particularly for the sessile benthic calcifiers that constitute
657 prey for mobile and upper trophic level taxa. For example, an experimental study on three
658 common Arctic bivalve species (*Macoma calcarean*, *Astarte montagui* and *Astarte borealis*)
659 collected in the CEO concluded that these species were generally resilient to decreasing pH
660 (Goethel et al., 2017). However, only two pH were compared (a "control" (pH of 8.1) and an
661 "acidified" treatment (pH of 7.8) and our results show that organisms are already experiencing
662 more extreme conditions today than have been experimentally manipulated. While these data
663 provide insights on these species' plasticity to present pH conditions, they cannot be used to infer
664 sensitivity to future ocean acidification or extremes of current conditions. Based on the local
665 adaptation hypothesis (Vargas et al. 2017, 2022), stress and associated negative effect on species

666 fitness can be expected when pH deviates from the extreme of the present range of variability
667 (pH<7.5) as shown in other regions (e.g. echinoderms: Dorey et al., (2013); crustaceans: Thor
668 and Dupont, (2015); bivalves: Ventura et al., (2016)).

669 At the CEO, our results show sustained periods of remarkably low pH (e.g., 7.5; summer
670 to fall, winter). Higher pH values are observed in spring and late fall. While we are lacking the
671 local biological data to sufficiently evaluate past and future ecosystem changes, a high rate of
672 ocean acidification as observed in the Chukchi Sea (Qi et al., 2022b, a), associated with potential
673 temperature-induced shifts in the carbonate chemistry cycle (e.g. Orr et al. 2022), have the
674 potential to impact species and ecosystems. Exposure to low pH increases organismal energy
675 requirements for maintenance (e.g. acid-base regulation: Stumpp et al., 2012, compensatory
676 calcification: Ventura et al., 2016). Organisms can cope with increased energy costs using a
677 variety of strategies, ranging from individual physiological to behavioral responses, depending
678 on trophic level, mobility, and other ecological factors. For example, they can use available
679 stored energy to compensate for increased costs or they can decrease their metabolism to limit
680 costs (AMAP 2018). At the CEO, the low pH period observed during the summer and fall is
681 associated with elevated temperature and an elevated food supply for herbivores (Lalande et al.,
682 2020). The high availability of food may then foster compensation for the higher energetic costs
683 associated with exposure to low pH. However, a longer period of low pH as suggested by our
684 data could lead to a mismatch between the low pH and food availability, with cascading negative
685 consequences for the ecosystem (Kroeker et al., 2021). In winter, the low pH conditions are
686 associated with low temperature, no light, and low food level concentrations. These conditions
687 are likely to keep metabolisms low and limit the negative effects of exposure to low pH
688 (Gianguzza et al., 2014). As food availability is limited by the absence of light, this strategy may

689 be compromised by an increase in temperature that could also lead to increased metabolism.
690 Additional work is needed to understand impacts of acidification conditions and variability on
691 the marine biota of the Chukchi Sea, including field and laboratory experiments that evaluate
692 biological response under realistic scenarios. The characterization of the environmental
693 conditions at the CEO, including the variability in time, can be used to design single and multiple
694 stressor experiments (carbonate chemistry, temperature, salinity, food, oxygen; Boyd et al.
695 2018).

696 Indigenous communities are at the forefront of the changing Arctic, including changes in
697 accessibility, availability, and condition of traditional marine foods (Buschman and Sudlovenick,
698 2022; Hauser et al., 2021). Several marine species are critical to the food and cultural security of
699 coastal Inupiat who have thrived in Arctic Alaska for millenia. While it is not possible to resolve
700 the consequences of the seasonal and interannual variations in carbonate chemistry documented
701 in this manuscript without a proper sensitivity evaluation, the seasonally low pH conditions have
702 the potential to impact organisms like bivalves in a foraging hotspot for walrus (Jay et al., 2012;
703 Kuletz et al., 2015). Walrus, as well as their bivalve stomach contents, are important nutritional,
704 spiritual, and cultural components, raising concerns for food security in the context of ecosystem
705 shifts associated with the variability and multiplicity of climate impacts within the region (ICC,
706 2015).

707

708 **5. Concluding Thoughts**

709 The Chukchi Sea is undergoing a rapid environmental transformation with potentially
710 far-reaching consequences across the ecosystem. While we are lacking a long-term time-series,
711 we used this dataset to investigate the drivers of extreme pH, Ω_{arag} , and $p\text{CO}_2$ and document

712 conditions that could affect the ecological niches of organisms, including a fast rate of ocean
713 acidification, elongated sea ice free periods, increased primary productivity and elevated
714 temperature. While a combination of experimental and monitoring approaches is needed for an
715 understanding of the ecological consequences of these changes, our results also highlight the
716 urgency to mitigate CO₂ emissions and simultaneously support Indigenous-led conservation
717 measures to safeguard an ecosystem in transition. Indigenous People in the Arctic have
718 established strategies to monitor, adapt to, and conserve the ecosystems upon which they depend.
719 Ethical and equitable engagement of Indigenous Knowledge and the communities at the forefront
720 of climate impacts can help guide research and conservation action by centering local priorities
721 and traditional practices, thereby supporting self-determination and sovereignty (Buschman and
722 Sudlovenick, 2022).

723

724 **Data availability**

725 The inorganic carbon data used in this manuscript are publicly available (Hauri and
726 Irving, 2023a; Hauri and Irving, 2023b).

727

728 **Author contributions**

729 CH and BI managed and serviced the HydroC CO₂ and SeapHOx sensors, analyzed and
730 published the data, and wrote the manuscript. SD and Peter Shipton carried out the CEO mooring
731 deployments and recoveries and managed and serviced the CTD and NO₃ sensors. RP, DH, SD,
732 and SLD contributed to the manuscript.

733

734 **Competing interests**

735 The authors have no competing interests.

736

737 **Acknowledgments**

738 The Chukchi Ecosystem Observatory is located on the traditional and contemporary
739 hunting grounds of the Northern Alaska Iñupiat. We also acknowledge that our Fairbanks-based
740 offices are located on the Native lands of the Lower Tanana Dena. The Indigenous Peoples of
741 this land never surrendered lands or resources to Russia or the United States. We acknowledge
742 this not only because we are grateful to the Indigenous communities who have been in deep
743 connection with the land and water for time immemorial, but also in recognition of the historical
744 and ongoing legacy of colonialism. We are committed to improving our scientific approaches
745 and working towards co-production for a better future for everyone.

746 We acknowledge the World Climate Research Programme, which, through its Working
747 Group on Coupled Modelling, coordinated and promoted CMIP6. We thank the climate
748 modeling groups for producing and making available their model output, the Earth System Grid
749 Federation (ESGF) for archiving the data and providing access, and the multiple funding
750 agencies who support CMIP6 and ESGF.

751

752 **Financial support**

753 We would like to thank the National Pacific Research Board Long-term Monitoring
754 (NPRB LTM) program (project no. 1426 and L-36), the Alaska Ocean Observing System (award
755 no. NA11NOS0120020 and NA16NOS0120027), and the University of Alaska Fairbanks for
756 their financial support. Claudine Hauri, Brita Irving, and Seth Danielson also acknowledge
757 support from the National Science Foundation Office of Ocean Sciences and Polar Programs

758 (OCE-1841948 and OPP-1603116). Projects that assisted in the servicing of the CEO and/or
759 collected water column calibration data were funded by the National Science Foundation, Bureau
760 of Ocean Energy Management, National Oceanic and Atmospheric Administration, National
761 Oceanographic Partnership Program, and Shell Exploration and Production Company, Inc.
762 Maintenance and calibration of the CEO sensors is only possible due to the kind support of
763 numerous collaborators within the Arctic research community who helped with CEO deployment
764 and recovery or collected sensor calibration samples. We would therefore like to thank Peter
765 Shipton, Carin Ashjian, Jessica Cross, Miguel Goñi, Jackie Grebmeier, Burke Hales, Katrin Iken,
766 Laurie Juranek, Calvin Mordy, and Robert Pickart.

767

768 **References**

769 Alin, S. R., Feely, R. A., Dickson, A. G., Hernández-Ayón, J. M., Juranek, L. W., Ohman, M.
770 D., and Goericke, R.: Robust empirical relationships for estimating the carbonate system in the
771 southern California Current System and application to CalCOFI hydrographic cruise data (2005–
772 2011), *Journal of Geophysical Research*, 117, C05033, doi:10.1029/2011JC007511, 2012.

773

774 AMAP. AMAP Assessment 2018: Arctic Ocean Acidification. Arctic Monitoring and
775 Assessment Programme (AMAP), Tromsø, Norway. vi+187pp,
776 [https://www.amap.no/documents/doc/AMAP-Assessment-2018-Arctic-Ocean-](https://www.amap.no/documents/doc/AMAP-Assessment-2018-Arctic-Ocean-Acidification/1659)
777 [Acidification/1659](https://www.amap.no/documents/doc/AMAP-Assessment-2018-Arctic-Ocean-Acidification/1659), 2018.

778

779 Arrigo, K. R. and van Dijken, G. L.: Continued increases in Arctic Ocean primary production,
780 *Prog. Oceanogr.*, 136, 60–70, <https://doi.org/10.1016/j.pocean.2015.05.002>, 2015.

781

782 Asahara, Y., Takeuchi, F., Nagashima, K., Harada, N., Yamamoto, K., Oguri, K., and Tadaï, O.:

783 Provenance of terrigenous detritus of the surface sediments in the Bering and Chukchi Seas as

784 derived from Sr and Nd isotopes: Implications for recent climate change in the Arctic regions,

785 *Deep Sea Res. Part II Top. Stud. Oceanogr.*, 61–64, 155–171,

786 <https://doi.org/10.1016/j.dsr2.2011.12.004>, 2012.

787

788 Bates, N.: Assessing ocean acidification variability in the Pacific-Arctic region as part of the

789 Russian-American Long-term Census of the Arctic, *Oceanography*, 28, 36–45,

790 <https://doi.org/10.5670/oceanog>, 2015.

791

792 Bates, N. R., Mathis, J. T. and Cooper, L. W.: Ocean acidification and biologically induced

793 seasonality of carbonate mineral saturation states in the western Arctic Ocean. *J. Geophys. Res.*

794 114, 2008JC004862, 2009.

795

796 Bednaršek, N., Calosi, P., Feely, R. A., Ambrose, R., Byrne, M., Chan, K. Y. K., Dupont, S.,

797 Padilla-Gamiño, J. L., Spicer, J. I., Kessouri, F., Roethler, M., Sutula, M., and Weisberg, S. B.:

798 Synthesis of thresholds of ocean acidification impacts on echinoderms, *Front. Mar. Sci.*,

799 8, <https://doi.org/10.3389/fmars.2021.602601>, 2021.

800

801 Bittig, H. C., Steinhoff, T., Claustre, H., Fiedler, B., Williams, N. L., Sauzède, R., Körtzinger,

802 A., and Gattuso, J.-P.: An alternative to static climatologies: robust estimation of open ocean

803 CO₂ variables and nutrient concentrations from T, S, and O₂ data using Bayesian neural
804 networks, *Front. Mar. Sci.*, 5, 328, <https://doi.org/10.3389/fmars.2018.00328>, 2018.
805

806 Blanchard, A. L., Parris, C. L., Knowlton, A. L. and Wade, N. R.: Benthic ecology of the
807 northeastern Chukchi Sea. Part I. Environmental characteristics and macrofaunal community
808 structure, 2008–2010. *Continental Shelf Research* 67, 52–66, 2013.
809

810 Boucher, O., Denvil, S., Levavasseur, G., Cozic, A., Caubel, A., Foujols, M.-A., Meurdesoif, Y.,
811 Balkanski, Y., Checa-Garcia, R., Hauglustaine, D., Bekki, S. and Marchand, M.: IPSL IPSL-
812 CM6A-LR-INCA model output prepared for CMIP6 AerChemMIP.
813 [doi:10.22033/ESGF/CMIP6.13581](https://doi.org/10.22033/ESGF/CMIP6.13581), 2020.
814

815 Boyd, P. W., Collins, S., Dupont, S., Fabricius, K., Gattuso, J.-P., Havenhand, J., Hutchins, D.
816 A., Riebesell, U., Rintoul, M. S., Vichi, M., Biswas, H., Ciotti, A., Gao, K., Gehlen, M., Hurd, C.
817 L., Kurihara, H., McGraw, C. M., Navarro, J. M., Nilsson, G. E., Passow, U. and Pörtner, H.-O.:
818 Experimental strategies to assess the biological ramifications of multiple drivers of global ocean
819 change—A review. *Global Change Biology* 24, 2239–2261, 2018.
820

821 Breitberg, D., Salisbury, J., Bernhard, J., Cai, W.-J., Dupont, S., Doney, S., Kroeker,
822 K., Levin, L.A., Long, W. C., Milke, L.M., Miller S.H., Phelan, B., Passow, U., Seibel,
823 B.A., Todgham, A.E., and Tarrant, A.M.: And on top of all that... Coping with ocean
824 acidification in the midst of many stressors. *Oceanography*, 25(2), 48–61.
825 <https://doi.org/10.5670/oceanog.2015.31>, 2015.

826

827 Bresnahan, P. J., Martz, T. R., Takeshita, Y., Johnson, K. S., and LaShomb, M.: Best practices
828 for autonomous measurement of seawater pH with the Honeywell Durafet, *Methods Oceanogr.*,
829 9, 44–60, <https://doi.org/10.1016/j.mio.2014.08.003>, 2014.

830

831 Brodzik, M. J. and K. W. Knowles: “Chapter 5: EASE-Grid: A Versatile Set of Equal-Area
832 Projections and Grids.” in Michael F. Goodchild (Ed.) *Discrete Global Grids: A Web Book*.
833 Santa Barbara, California USA: National Center for Geographic Information & Analysis.
834 <https://escholarship.org/uc/item/9492q6sm>, 2002.

835

836 Buschman, V. Q. and Sudlovenick, E.: Indigenous-led conservation in the Arctic supports global
837 conservation practices, *Arctic Science*, 9(3): 714-719, <https://doi.org/10.1139/as-2022-0025>,
838 2022.

839

840 Carmack, E. and Wassmann, P.: Food webs and physical–biological coupling on pan-Arctic
841 shelves: unifying concepts and comprehensive perspectives. *Progress in Oceanography*, 71(2-4),
842 pp.446-477, 2006.

843

844 Carter, B. R., Feely, R. A., Williams, N. L., Dickson, A. G., Fong, M. B., and Takeshita, Y.:
845 Updated methods for global locally interpolated estimation of alkalinity, pH, and nitrate,
846 *Methods Limnology and Oceanography*, 16(2), 119-131, <https://doi.org/10.1002/lom3.10232>,
847 2018.

848

849 Chatterjee, S., and Hadi, A. S.: “Influential Observations, High Leverage Points, and Outliers in
850 Linear Regression.” *Statistical Science*, 1(3), 1986, pp. 379–416, 10.1214/ss/1177013622, 1986.
851

852 Corlett, W. B. and Pickart, R. S.: The Chukchi slope current. *Progress in Oceanography* 153, 50–
853 65, 2017.
854

855 Cross, J. N., Mathis, J. T., Bates, N. R., and Byrne, R. H.: Conservative and non-conservative
856 variations of total alkalinity on the Southeastern Bering Sea Shelf, *Mar. Chem.*, 154, 100–112,
857 <https://doi.org/10.1016/j.marchem.2013.05.012>, 2013.
858

859 Cross, J. N., Monacci, N. M., Bell, S. W., Grebmeier, J. M., Mordy, C., Pickart, R. S., Stabeno,
860 and P. J.: Dissolved inorganic carbon (DIC), total alkalinity (TA) and other variables collected
861 from discrete samples and profile observations from United States Coast Guard Cutter (USCGC)
862 Healy cruise HLY1702 (EXPOCODE 33HQ20170826) in the Bering and Chukchi Sea along
863 transect lines in the Distributed Biological Observatory (DBO) from 2017-08-26 to 2017-09-15
864 (NCEI Accession 0208337). NOAA National Centers for Environmental Information. Dataset.
865 <https://doi.org/10.25921/pks4-4p43>, 2020a.
866

867 Cross, J. N., Monacci, N. M., Bell, S. W., Grebmeier, J. M., Mordy, C., Pickart, R. S., and
868 Stabeno, P. J.: Dissolved inorganic carbon (DIC), total alkalinity (TA) and other parameters
869 collected from discrete sample and profile observations during the USCGC Healy cruise
870 HLY1801 (EXPOCODE 33HQ20180807) in the Bering Sea, Chukchi Sea and Beaufort Sea
871 along transect lines in the Distributed Biological Observatory (DBO) from 2018-08-07 to 2018-

872 08-24 (NCEI Accession 0221911). NOAA National Centers for Environmental Information.
873 Dataset. <https://doi.org/10.25921/xc4b-xh20>, 2020b.
874
875 Cross, J. N., Monacci, N. M., Bell, S. W., Grebmeier, J. M., Mordy, C., Pickart, Robert S.,
876 Stabeno, P.J.: Dissolved inorganic carbon (DIC) and total alkalinity (TA) and other hydrographic
877 and chemical data collected from discrete sample and profile observations during the United
878 States Coast Guard Cutter (USCGC) Healy cruise HLY1901 (EXPOCODE 33HQ20190806) in
879 the Bering and Chukchi Sea along transect lines in the Distributed Biological Observatory
880 (DBO) from 2019-08-06 to 2019-08-22 (NCEI Accession 0243277). NOAA National Centers for
881 Environmental Information. Dataset. <https://doi.org/10.25921/b5s5-py61>, 2021.
882
883 Cullison-Gray, S. E., DeGrandpre, M. D., Moore, T. S., Martz, T. R., Friederich, G. E., and
884 Johnson, K. S.: Applications of in situ pH measurements for inorganic carbon calculations, *Mar.*
885 *Chem.*, 125, 82–90, <https://doi.org/10.1016/j.marchem.2011.02.005>, 2011.
886
887 Daniel, A., Laës-Huon, A., Barus, C., Beaton, A. D., Blandfort, D., Guigues, N., Knockaert, M.,
888 Munaron, D., Salter, I., Woodward, E. M. S., Greenwood, N., and Achterberg, E. P.: Toward a
889 harmonization for using in situ nutrient sensors in the marine environment, *Front. Mar. Sci.*, 6,
890 773, <https://doi.org/10.3389/fmars.2019.00773>, 2020.
891
892 Danielson, S.L., Iken, K., Hauri, C., Hopcroft, R.R., McDonnell, A.M., Winsor, P., Lalande, C.,
893 Grebmeier, J.M., Cooper, L.W., Horne, J.K. and Stafford, K.M.: Collaborative approaches to

894 multi-disciplinary monitoring of the Chukchi shelf marine ecosystem: Networks of networks for
895 maintaining long-term Arctic observations. In OCEANS 2017-Anchorage (pp. 1-7). IEEE, 2017.

896

897 Danielson, S. L., Ahkinga, O., Ashjian, C., Basyuk, E., Cooper, L. W., Eisner, L., Farley, E.,
898 Iken, K. B., Grebmeier, J. M., Juranek, L., Khen, G., Jayne, S. R., Kikuchi, T., Ladd, C., Lu, K.,
899 McCabe, R. M., Moore, G. W. K., Nishino, S., Ozenna, F., Pickart, R. S., Polyakov, I., Stabeno,
900 P. J., Thoman, R., Williams, W. J., Wood, K., and Weingartner, T. J.: Manifestation and
901 consequences of warming and altered heat fluxes over the Bering and Chukchi Sea continental
902 shelves, *Deep Sea Res. Part II Top. Stud. Oceanogr.*, 177, 104781,
903 <https://doi.org/10.1016/j.dsr2.2020.104781>, 2020.

904

905 Danielson, S.: Water temperature, conductivity, and others taken by CTD and Niskin bottles
906 from the research vessel Norseman II Data for Arctic Marine Biodiversity Observing Network,
907 AMBON, Program in the Chukchi Sea from 2017-08-07 to 2017-08-22 (NCEI Accession
908 0229072). NOAA National Centers for Environmental Information. Dataset.
909 <https://doi.org/10.25921/afz7-0d98>, 2021.

910

911 DeGrandpre, M. D., Lai, C.-Z., Timmermans, M.-L., Krishfield, R. A., Proshutinsky, A. and
912 Torres, D.: Inorganic Carbon and pCO₂ Variability During Ice Formation in the Beaufort Gyre of
913 the Canada Basin. *Journal of Geophysical Research: Oceans* 124, 4017–4028, 2019.

914

915 Dickson, A. G.: Thermodynamics of the dissociation of boric acid in synthetic seawater from
916 273.15 to 318.15 K, *Deep Sea Res. Part Oceanogr. Res. Pap.*, 37, 755–766,
917 [https://doi.org/10.1016/0198-0149\(90\)90004-F](https://doi.org/10.1016/0198-0149(90)90004-F), 1990.
918
919 Dickson, A. G., Sabine, C. L., and Christian, J. R.: Guide to best practices for ocean CO₂
920 measurements, PICES, Sydney, 191 pp., 2007.
921
922 DiGirolamo, N. E., C. L. Parkinson, D. J. Cavalieri, P. Gloersen, and H. J. Zwally: Sea Ice
923 Concentrations from Nimbus-7 SMMR and DMSP SSM/I-SSMIS Passive Microwave Data,
924 Version 2. Boulder, Colorado USA. NASA National Snow and Ice Data Center Distributed
925 Active Archive Center. <https://doi.org/10.5067/MPYG15WAA4WX>, 2022.
926
927 Dorey, N., Lançon, P., Thorndyke, M., and Dupont, S.: Assessing physiological tipping point of
928 sea urchin larvae exposed to a broad range of pH, *Glob. Change Biol.*, 19, 3355–3367,
929 <https://doi.org/10.1111/gcb.12276>, 2013.
930
931 Doney, S. C., Busch, D. S., Cooley, S. R. and Kroeker, K. J.: The Impacts of Ocean
932 Acidification on Marine Ecosystems and Reliant Human Communities. *Annu. Rev. Environ.*
933 *Resour.* 45, 83–112, 2020.
934
935 Duke, P. J., Else, B. G. T., Jones, S. F., Marriot, S., Ahmed, M. M. M., Nandan, V., Butterworth,
936 B., Gonski, S. F., Dewey, R., Sastri, A., Miller, L. A., Simpson, K. G., and Thomas, H.: Seasonal
937 marine carbon system processes in an Arctic coastal landfast sea ice environment observed with

938 an innovative underwater sensor platform, *Elementa: Science of the Anthropocene*, 9 (1): 00103,
939 <https://doi.org/10.1525/elementa.2021.00103>, 2021.

940

941 Etminan, M., Myhre, G., Highwood, E. J., and Shine, K. P.: Radiative forcing of carbon dioxide,
942 methane, and nitrous oxide: A significant revision of the methane radiative forcing, *Geophys.*
943 *Res. Lett.*, 43, 12,614-12,623, <https://doi.org/10.1002/2016GL071930>, 2016.

944

945 Fang, Y.C., Weingartner, T.J., Dobbins, E.L., Winsor, P., Statscewich, H., Potter, R.A., Mudge,
946 T.D., Stoudt, C.A. and Borg, K.: Circulation and thermohaline variability of the Hanna Shoal
947 region on the northeastern Chukchi Sea shelf. *Journal of Geophysical Research: Oceans*, 125(7),
948 p.e2019JC015639, 2020.

949

950 Fietzek, P., Fiedler, B., Steinhoff, T., and Körtzinger, A.: In situ quality assessment of a novel
951 underwater CO₂ sensor based on membrane equilibration and NDIR spectrometry, *J.*
952 *Atmospheric Ocean. Technol.*, 31, 181–196, <https://doi.org/10.1175/JTECH-D-13-00083.1>,
953 2014.

954

955 Friis, K.: The salinity normalization of marine inorganic carbon chemistry data, *Geophys. Res.*
956 *Lett.*, 30, 1085, <https://doi.org/10.1029/2002GL015898>, 2003.

957

958 Gianguzza, P., Visconti, G., Gianguzza, F., Vizzini, S., Sarà, G., and Dupont, S.: Temperature
959 modulates the response of the thermophilous sea urchin *Arbacia lixula* early life stages to CO₂-

960 driven acidification, *Mar. Environ. Res.*, 93, 70–77,
961 <https://doi.org/10.1016/j.marenvres.2013.07.008>, 2014.
962
963 Goethel, C. L., Grebmeier, J. M., Cooper, L. W., and Miller, T. J.: Implications of ocean
964 acidification in the Pacific Arctic: Experimental responses of three Arctic bivalves to decreased
965 pH and food availability, *Deep Sea Res. Part II Top. Stud. Oceanogr.*, 144, 112–124,
966 <https://doi.org/10.1016/j.dsr2.2017.08.013>, 2017.
967
968 Gonzalez, S., Home, J. K., and Danielson, S. L.: Multi-scale temporal variability in biological-
969 physical associations in the NE Chukchi Sea, *Polar Biol.*, 44, 837–855,
970 <https://doi.org/10.1007/s00300-021-02844-1>, 2021.
971
972 Grebmeier, J. M., Bluhm, B. A., Cooper, L. W., Danielson, S. L., Arrigo, K. R., Blanchard, A.
973 L., Clarke, J. T., Day, R. H., Frey, K. E., Gradinger, R. R., Kędra, M., Konar, B., Kuletz, K. J.,
974 Lee, S. H., Lovvorn, J. R., Norcross, B. L. and Okkonen, S. R.: Ecosystem characteristics and
975 processes facilitating persistent macrobenthic biomass hotspots and associated benthivory in the
976 Pacific Arctic. *Progress in Oceanography* 136, 92–114,
977 <https://doi.org/10.1016/j.pocean.2015.05.006>, 2015.
978
979 Hauri, C., Gruber, N., Vogt, M., Doney, S. C., Feely, R. A., Lachkar, Z., Leinweber, A.,
980 McDonnell, A. M. P., Munnich, M. and Plattner, G.-K.: Spatiotemporal variability and long-term
981 trends of ocean acidification in the California Current System. *Biogeosciences* 10, 193–216,
982 <https://doi.org/10.5194/bg-10-193-2013>, 2013.

983

984 Hauri, C., Danielson, S., McDonnell, A. M. P., Hopcroft, R. R., Winsor, P., Shipton, P., Lalande,
985 C., Stafford, K. M., Horne, J. K., Cooper, L. W., Grebmeier, J. M., Mahoney, A., Maisch, K.,
986 McCammon, M., Statscewich, H., Sybrandy, A., and Weingartner, T.: From sea ice to seals: a
987 moored marine ecosystem observatory in the Arctic, *Ocean Sci.*, 14, 1423–1433,
988 <https://doi.org/10.5194/os-14-1423-2018>, 2018.

989

990 Hauri, C., Pagès, R., McDonnell, A. M. P., Stuecker, M. F., Danielson, S. L., Hedstrom, K.,
991 Irving, B., Schultz, C., and Doney, S. C.: Modulation of ocean acidification by decadal climate
992 variability in the Gulf of Alaska, *Communications Earth & Environment* 2, 191,
993 <https://doi.org/10.1038/s43247-021-00254-z>, 2021.

994

995 Hauri, C. and Irving, B.: pCO₂ time series measurements from the Chukchi Ecosystem
996 Observatory CEO2 mooring deployed at 33 meters depth in the Northeast Chukchi Sea. Research
997 Workspace. <https://doi.org/10.24431/rw1k7dq>,
998 version: 10.24431_rw1k7dq_20230531T123002Z, 2023a.

999

1000 Hauri, C. and Irving, B.: pH, temperature, salinity, and oxygen time series measurements from
1001 the Chukchi Ecosystem Observatory CEO2 mooring deployed at 33 meters depth in the
1002 Northeast Chukchi Sea. Research Workspace. <https://doi.org/10.24431/rw1k7dp>,
1003 version: 10.24431_rw1k7dp_20230531T121136Z, 2023b.

1004

1005 Hauser, D. D. W., Whiting, A. V., Mahoney, A. R., Goodwin, J., Harris, C., Schaeffer, R. J.,
1006 Schaeffer, R., Laxague, N. J. M., Subramaniam, A., Witte, C. R., Betcher, S., Lindsay, J. M., and
1007 Zappa, C. J.: Co-production of knowledge reveals loss of Indigenous hunting opportunities in the
1008 face of accelerating Arctic climate change, *Environ. Res. Lett.*, 16, 095003,
1009 <https://doi.org/10.1088/1748-9326/ac1a36>, 2021.
1010
1011 Hayes, D., Kemme, J., and Hauri C.: Ocean greenhouse gas monitoring: new autonomous
1012 platform to measure pCO₂, methane, *Sea Technology*, 63(10), 13-16, [https://lsc-](https://lsc-pagepro.mydigitalpublication.com/publication/?i=764237&p=13&view=issueViewer)
1013 [pagepro.mydigitalpublication.com/publication/?i=764237&p=13&view=issueViewer](https://lsc-pagepro.mydigitalpublication.com/publication/?i=764237&p=13&view=issueViewer), 2022.
1014
1015 Hennon, T. D., Danielson, S. L., Woodgate, R. A., Irving, B., Stockwell, D. A., and Mordy, C.
1016 W.: Mooring Measurements of Anadyr Current Nitrate, Phosphate, and Silicate Enable Updated
1017 Bering Strait Nutrient Flux Estimates, *Geophys. Res. Lett.*, 49, e2022GL098908,
1018 <https://doi.org/10.1029/2022GL098908>, 2022.
1019
1020 Holmes, R.M., J.W. McClelland, S.E. Tank, R.G.M. Spencer, and A.I. Shiklomanov.: Arctic
1021 Great Rivers Observatory. Water Quality Dataset, <https://www.arcticgreatrivers.org/data>, 2021.
1022
1023 Horowitz, L. W., Naik, V., Sentman, L., Paulot, F., Blanton, C., McHugh, C., Radhakrishnan, A.,
1024 Rand, K., Vahlenkamp, H., Zadeh, N. T., Wilson, C., Ginoux, P., He, J., John, J. G., Lin, M.,
1025 Paynter, D. J., Ploshay, J., Zhang, A. and Zeng, Y.: NOAA-GFDL GFDL-ESM4 model output
1026 prepared for CMIP6 AerChemMIP hist-1950HC. doi:10.22033/ESGF/CMIP6.8568, 2018.
1027

1028 Huntington, H. P., Danielson, S. L., Wiese, F. K., Baker, M., Boveng, P., Citta, J. J., De
1029 Robertis, A., Dickson, D. M. S., Farley, E., George, J. C., Iken, K., Kimmel, D. G., Kuletz, K.,
1030 Ladd, C., Levine, R., Quakenbush, L., Stabeno, P., Stafford, K. M., Stockwell, D., and Wilson,
1031 C.: Evidence suggests potential transformation of the Pacific Arctic ecosystem is underway, *Nat.*
1032 *Clim. Change*, 10, 342–348, <https://doi.org/10.1038/s41558-020-0695-2>, 2020.
1033
1034 Huntington, H. P., Zagorsky, A., Kaltenborn, B. P., Shin, H. C., Dawson, J., Lukin, M., Dahl, P.
1035 E., Guo, P., and Thomas, D. N.: Societal implications of a changing Arctic Ocean. *Ambio*, 51(2),
1036 298–306. <https://doi.org/10.1007/s13280-021-01601-2>, 2022.
1037
1038 ICC: Alaskan Inuit food security conceptual framework: how to assess the Arctic from an Inuit
1039 perspective, Inuit Circumpolar Council-Alaska, Anchorage, 2015.
1040
1041 Irving, B., SUNA_V2_processing, GitHub repository, https://github.com/britairving/SUNA_V2,
1042 2021.
1043
1044 Islam, F., DeGrandpre, M. D., Beatty, C.M., Timmermanns, M.-L., Krishfield, R. A., Toole,
1045 J.M., and Laney, S.R.: Sea surface pCO₂ and O₂ dynamics in the partially ice-covered Arctic
1046 Ocean, *JGR Oceans*, 122(2), 1425-1438, <https://doi.org/10.1002/2016JC012162>, 2017.
1047
1048 Jay, C. V., Fischbach, A. S., and Kochnev, A. A.: Walrus areas of use in the Chukchi Sea during
1049 sparse sea ice cover, *Mar. Ecol. Prog. Ser.*, 468, 1–13, <https://doi.org/10.3354/meps10057>, 2012.
1050

Deleted: 6

1052 Jiang, L.-Q., Feely, R. A., Wanninkhof, R., Greeley, D., Barbero, L., Alin, S., Carter, B. R.,
1053 Pierrot, D., Featherstone, C., Hooper, J., Melrose, C., Monacci, N., Sharp, J. D., Shellito, S., Xu,
1054 Y.-Y., Kozyr, A., Byrne, R. H., Cai, W.-J., Cross, J., Johnson, G. C., Hales, B., Langdon, C.,
1055 Mathis, J., Salisbury, J., and Townsend, D. W.: Coastal Ocean Data Analysis Product in North
1056 America (CODAP-NA) – an internally consistent data product for discrete inorganic carbon,
1057 oxygen, and nutrients on the North American ocean margins, *Earth Syst. Sci. Data*, 13, 2777–
1058 2799, <https://doi.org/10.5194/essd-13-2777-2021>, 2021.

1059

1060 Jung, J., Son, J. E., Lee, Y. K., Cho, K.-H., Lee, Y., Yang, E. J., Kang, S.-H., and Hur, J.:
1061 Tracing riverine dissolved organic carbon and its transport to the halocline layer in the Chukchi
1062 Sea (western Arctic Ocean) using humic-like fluorescence fingerprinting, *Sci. Total Environ.*,
1063 772, 145542, <https://doi.org/10.1016/j.scitotenv.2021.145542>, 2021.

1064

1065 Juranek, L. W., Feely, R. A., Peterson, W. T., Alin, S. R., Hales, B., Lee, K., Sabine, C. L., and
1066 Peterson, J.: A novel method for determination of aragonite saturation state on the continental
1067 shelf of central Oregon using multi-parameter relationships with hydrographic data, *Geophys.*
1068 *Res. Lett.*, 36, L24601, <https://doi.org/10.1029/2009GL040778>, 2009.

1069

1070 Juranek, L. W., Feely, R. A., Gilbert, D., Freeland, H., and Miller, L. A.: Real-time estimation of
1071 pH and aragonite saturation state from Argo profiling floats: Prospects for an autonomous carbon
1072 observing strategy, *Geophys. Res. Lett.*, 38, L17603, <https://doi.org/10.1029/2011gl048580>,
1073 2011.

1074

1075 Koch, C. W., Cooper, L. W., Lalande, C., Brown, T. A., Frey, K. E. and Grebmeier, J. M.:
1076 Seasonal and latitudinal variations in sea ice algae deposition in the Northern Bering and
1077 Chukchi Seas determined by algal biomarkers. *PLoS ONE* 15, e0231178, 2020.
1078
1079 Kroeker, K. J., Powell, C., and Donham, E. M.: Windows of vulnerability: Seasonal mismatches
1080 in exposure and resource identity determine ocean acidification's effect on a primary consumer
1081 at high latitude, *Glob. Change Biol.*, 27, 1042–1051, <https://doi.org/10.1111/gcb.15449>, 2021.
1082
1083 Kuletz, K. J., Ferguson, M. C., Hurley, B., Gall, A. E., Labunski, E. A., and Morgan, T. C.:
1084 Seasonal spatial patterns in seabird and marine mammal distribution in the eastern Chukchi and
1085 western Beaufort seas: Identifying biologically important pelagic areas, *Prog. Oceanogr.*, 136,
1086 175–200, <https://doi.org/10.1016/j.pocean.2015.05.012>, 2015.
1087
1088 Lalande, C., Grebmeier, J. M., Hopcroft, R. R., and Danielson, S. L.: Annual cycle of export
1089 fluxes of biogenic matter near Hanna Shoal in the northeast Chukchi Sea, *Deep Sea Res. Part II*
1090 *Top. Stud. Oceanogr.*, 177, 104730, <https://doi.org/10.1016/j.dsr2.2020.104730>, 2020.
1091
1092 Lalande, C., Grebmeier, J. M., McDonnell, A. M. P., Hopcroft, R. R., O'Daly, S., and Danielson,
1093 S. L.: Impact of a warm anomaly in the Pacific Arctic region derived from time-series export
1094 fluxes, *PLOS ONE*, 16, e0255837, <https://doi.org/10.1371/journal.pone.0255837>, 2021.
1095
1096 Lauvset, S. K., Lange, N., Tanhua, T., Bittig, H. C., Olsen, A., Kozyr, A., Álvarez, M., Becker,
1097 S., Brown, P. J., Carter, B. R., Cotrim da Cunha, L., Feely, R. A., van Heuven, S., Hoppema, M.,

1098 Ishii, M., Jeansson, E., Jutterström, S., Jones, S. D., Karlsen, M. K., Lo Monaco, C., Michaelis,
1099 P., Murata, A., Pérez, F. F., Pfeil, B., Schirmick, C., Steinfeldt, R., Suzuki, T., Tilbrook, B., Velo,
1100 A., Wanninkhof, R., Woosley, R. J., and Key, R. M.: An updated version of the global interior
1101 ocean biogeochemical data product, GLODAPv2.2021, Earth Syst. Sci. Data Discuss.,
1102 <https://doi.org/10.5194/essd-2021-234>, 2021.

1103

1104 Laws, E. A.: Photosynthetic quotients, new production and net community production in the
1105 open ocean, Deep Sea Res. Part Oceanogr. Res. Pap., 38, 143–167, [https://doi.org/10.1016/0198-](https://doi.org/10.1016/0198-0149(91)90059-O)
1106 [0149\(91\)90059-O](https://doi.org/10.1016/0198-0149(91)90059-O), 1991.

1107

1108 Lee, K., Kim, T.-W., Byrne, R. H., Millero, F. J., Feely, R. A., and Liu, Y.-M.: The universal
1109 ratio of boron to chlorinity for the North Pacific and North Atlantic oceans, Geochim.
1110 Cosmochim. Acta, 74, 1801–1811, <https://doi.org/10.1016/j.gca.2009.12.027>, 2010.

1111

1112 Lewis, E. and Wallace, D. W. R.: Program Developed for CO₂ System Calculations,
1113 ORNL/CDIAC-105, Carbon Dioxide Inf. Anal. Cent., Oak Ridge Natl. Lab., Oak Ridge, Tenn.,
1114 38 pp., <https://salish-sea.pnnl.gov/media/ORNL-CDIAC-105.pdf>, 1998.

1115

1116 Lewis, K. M., van Dijken, G. L., and Arrigo, K. R.: Changes in phytoplankton concentration now
1117 drive increased Arctic Ocean primary production, Science, 369, 198–202,
1118 <https://doi.org/10.1126/science.aay8380>, 2020.

1119

1120 Li, B., Watanabe, Y. W., and Yamaguchi, A.: Spatiotemporal distribution of seawater pH in the
1121 North Pacific subpolar region by using the parameterization technique, *J. Geophys. Res. Oceans*,
1122 121, 3435–3449, <https://doi.org/10.1002/2015JC011615>, 2016.

1123

1124 Licker, R., Ekwurzel, B., Doney, S. C., Cooley, S. R., Lima, I. D., Heede, R., and Frumhoff, P.
1125 C.: Attributing ocean acidification to major carbon producers, *Environ. Res. Lett.*, 14, 124060,
1126 <https://doi.org/10.1088/1748-9326/ab5abc>, 2019.

1127

1128 Lueker, T. J., Dickson, A. G., and Keeling, C. D.: Ocean pCO₂ calculated from dissolved
1129 inorganic carbon, alkalinity, and equations for K₁ and K₂: validation based on laboratory
1130 measurements of CO₂ in gas and seawater at equilibrium, *Mar. Chem.*, 70, 105–119,
1131 [https://doi.org/10.1016/S0304-4203\(00\)00022-0](https://doi.org/10.1016/S0304-4203(00)00022-0), 2000.

1132

1133 Mathis, J. T. and Questel, J. M.: Assessing seasonal changes in carbonate parameters across
1134 small spatial gradients in the Northeastern Chukchi Sea. *Continental Shelf Research* 67, 42–51,
1135 <https://doi.org/10.1016/j.csr.2013.04.041>, 2013.

1136

1137 Martz, T. R., Connery, J. G., and Johnson, K. S.: Testing the Honeywell Durafet for seawater pH
1138 applications, *Limnol. Oceanogr. Methods*, 8, 172–184, <https://doi.org/10.4319/lom.2010.8.172>,
1139 2010.

1140

1141 Mauritsen, T., Bader, J., Becker, T., Behrens, J., Bittner, M., Brokopf, R., Brovkin, V., Claussen,
1142 M., Crueger, T., Esch, M., Fast, I., Fiedler, S., Fläschner, D., Gayler, V., Giorgetta, M., Goll, D.

1143 S., Haak, H., Hagemann, S., Hedemann, C., Hohenegger, C., Ilyina, T., Jahns, T., Jimenéz-de-la-
1144 Cuesta, D., Jungclaus, J., Kleinen, T., Kloster, S., Kracher, D., Kinne, S., Kleberg, D., Lasslop,
1145 G., Kornbluh, L., Marotzke, J., Matei, D., Meraner, K., Mikolajewicz, U., Modali, K., Möbis,
1146 B., Müller, W. A., Nabel, J. E. M. S., Nam, C. C. W., Notz, D., Nyawira, S.-S., Paulsen, H.,
1147 Peters, K., Pincus, R., Pohlmann, H., Pongratz, J., Popp, M., Raddatz, T. J., Rast, S., Redler, R.,
1148 Reick, C. H., Rohrschneider, T., Schemann, V., Schmidt, H., Schnur, R., Schulzweida, U., Six,
1149 K. D., Stein, L., Stemmler, I., Stevens, B., von Storch, J.-S., Tian, F., Voigt, A., Vrese, P.,
1150 Wieners, K.-H., Wilkenskield, S., Winkler, A., and Roeckner, E.: Developments in the MPI-M
1151 Earth System Model version 1.2 (MPI-ESM1.2) and Its Response to Increasing CO₂, *J. Adv.*
1152 *Model. Earth Syst.*, 11, 998–1038, <https://doi.org/10.1029/2018MS001400>, 2019.

1153

1154 McDougall, T.J. and Barker, P.M.: Getting started with TEOS-10 and the Gibbs Seawater
1155 (GSW) Oceanographic Toolbox, 28pp., SCOR/IAPSO WG127, ISBN 978-0-646-55621-5, 2011.

1156

1157 McRaven, L. and Pickart, R.: Conductivity-Temperature-Depth (CTD) data from the 2018
1158 Distributed Biological Observatory - Northern Chukchi Integrated Study (DBO-NCIS) cruise on
1159 USCGC (US Coast Guard Cutter) Healy (HLY1801). Arctic Data Center.
1160 doi:10.18739/A2HT2GC7Z, 2021.

1161

1162 Monacci, N. M., Cross, J. N., Pickart, R. S., Juranek, L. W., McRaven, L. T., and Becker, S.:
1163 Dissolved inorganic carbon (DIC) and total alkalinity (TA) and other hydrographic and chemical
1164 data collected from discrete sample and profile observations aboard the RV Sikuliaq Cruise
1165 SKQ202014S (EXPOCODE 33BI20201025) in the Bering and Chukchi Sea along transect lines

1166 in the Distributed Biological Observatory (DBO) from 2020-10-25 to 2020-11-11 (NCEI
1167 Accession 0252613). NOAA National Centers for Environmental Information. Dataset.
1168 <https://doi.org/10.25921/pnsd-sv10>, 2022.
1169
1170 Moore, S. E., Douglas P. deMaster, and Paul K. Dayton: Cetacean Habitat Selection in the
1171 Alaskan Arctic during Summer and Autumn, *Arctic*, 53(4), 432–47. JSTOR,
1172 <http://www.jstor.org/stable/40512256>, 2000.
1173
1174 Moore, S. E., and Stabeno, P. J.: Synthesis of Arctic Research (SOAR) in marine ecosystems of
1175 the Pacific Arctic, *Progress in Oceanography*, 136, 1-11,
1176 <https://doi.org/10.1016/j.pocean.2015.05.017>, 2015,
1177
1178 Moore, S. E., Clarke, J. T., Okkonen, S. R., Grebmeier, J. M., Berchok, C. L., and Stafford, K.
1179 M.: Changes in gray whale phenology and distribution related to prey variability and ocean
1180 biophysics in the northern Bering and eastern Chukchi seas. *PLOS ONE* 17(4):
1181 e0265934. <https://doi.org/10.1371/journal.pone.0265934>, 2022.
1182
1183 Mordy, C. W., Bell, S., Cokelet, E. D., Ladd, C., Lebon, G., Proctor, P., Stabeno, P., Strausz, D.,
1184 Wisegarver, E., and Wood, K.: Seasonal and interannual variability of nitrate in the eastern
1185 Chukchi Sea: Transport and winter replenishment, *Deep-Sea Res. Part II Top. Stud. Oceanogr.*,
1186 177, 104807, <https://doi.org/10.1016/j.dsr2.2020.104807>, 2020.
1187

1188 National Academies of Sciences, Engineering and Medicine: Valuing Climate Damages:
1189 Updating Estimation of the Social Cost of Carbon Dioxide (Washington DC: The National
1190 Academies Press) <https://doi.org/10.17226/24651>, 2017.
1191
1192 Newton, J. A., Feely, R. A., Jewett, E. B., Williamson, P., and Mathis, J.: Global ocean
1193 acidification observing network: requirements and governance plan, GOA-ON, Washington, 61
1194 pp., http://www.goa-on.org/docs/GOA-ON_plan_print.pdf, 2015.
1195
1196 Orr, J. C.: Recent and future changes in ocean carbonate chemistry, in: Ocean acidification,
1197 edited by: Gattuso, J.-P. and Hansson, L., Oxford University Press, Oxford, 41–66, 2011.
1198
1199 Orr, J. C., Epitalon, J.-M., Dickson, A. G., and Gattuso, J.-P.: Routine uncertainty propagation
1200 for the marine carbon dioxide system, *Mar. Chem.*, 207, 84–107,
1201 <https://doi.org/10.1016/j.marchem.2018.10.006>, 2018.
1202
1203 Orr, J. C., Kwiatkowski, L., and Pörtner, H. O.: Arctic Ocean annual high in pCO₂ could shift
1204 from winter to summer, *Nature*, 610, 94–100, <https://doi.org/10.1038/s41586-022-05205-y>,
1205 2022.
1206
1207 Ouyang, Z., Collins, A., Li, Y., Qi, D., Arrigo, K. R., Zhuang, Y., Nishino, S., Humphreys, M.
1208 P., Kosugi, N., Murata, A., Kirchman, D. L., Chen, L., Chen, J. and Cai, W.-J.: Seasonal Water
1209 Mass Evolution and Non-Redfield Dynamics Enhance CO₂ Uptake in the Chukchi Sea. *Journal*
1210 *of Geophysical Research: Oceans* 127, e2021JC018326,

1211 <https://doi.org/10.1029/2021JC018326>, 2022.
1212
1213 Payne, C. M., Bianucci, L., van Dijken, G. L., and Arrigo, K. R.: Changes in Under-Ice Primary
1214 Production in the Chukchi Sea From 1988 to 2018, *J. Geophys. Res. Oceans*, 126,
1215 e2021JC017483, <https://doi.org/10.1029/2021JC017483>, 2021.
1216
1217 Perez, F. F. and Fraga, F.: Association constant of fluoride and hydrogen ions in seawater, *Mar.*
1218 *Chem.*, 21, 161–168, [https://doi.org/10.1016/0304-4203\(87\)90036-3](https://doi.org/10.1016/0304-4203(87)90036-3), 1987.
1219
1220 Pipko, I. I., Semiletov, I. P., Tishchenko, P. Y., Pugach, S. P. and Christensen, J. P.: Carbonate
1221 chemistry dynamics in Bering Strait and the Chukchi Sea. *Progress in Oceanography* 55, 77–94,
1222 [https://doi.org/10.1016/S0079-6611\(02\)00071-X](https://doi.org/10.1016/S0079-6611(02)00071-X), 2 002.
1223
1224 Qi, D., Chen, L., Chen, B., Gao, Z., Zhong, W., Feely, R. A., Anderson, L. G., Sun, H., Chen, J.,
1225 Chen, M., Zhan, L., Zhang, Y., and Cai, W.-J.: Increase in acidifying water in the western Arctic
1226 Ocean, *Nat. Clim. Change*, 7, 195–199, <https://doi.org/10.1038/nclimate3228>, 2017.
1227
1228 Qi, D., Ouyang, Z., Chen, L., Wu, Y., Lei, R., Chen, B., Feely, R. A., Anderson, L. G., Zhong,
1229 W., Lin, H., Polukhin, A., Zhang, Y., Zhang, Y., Bi, H., Lin, X., Luo, Y., Zhuang, Y., He, J.,
1230 Chen, J., and Cai, W. J.: Climate change drives rapid decadal acidification in the Arctic Ocean
1231 from 1994 to 2020, *Science*, 377, 1544–1550, <https://doi.org/10.1126/science.abo0383>, 2022a.
1232

1233 Qi, D., Wu, Y., Chen, L., Cai, W.-J., Ouyang, Z., Zhang, Y., Anderson, L. G., Feely, R. A.,
1234 Zhuang, Y., Lin, H., Lei, R., and Bi, H.: Rapid acidification of the Arctic Chukchi Sea waters
1235 driven by anthropogenic forcing and biological carbon recycling, *Geophysical Research Letter*,
1236 49(4), e2021GL097246, <https://doi.org/10.1029/2021GL097246>, 2022b.

1237

1238 Raimondi, L., Matthews, J. B. R., Atamanchuck, D., Azetsu-Scott, K., and Wallace, D.: The
1239 internal consistency of the marine carbon dioxide system for high latitude shipboard and in situ
1240 monitoring, *Mar. Chem.*, 213, 49–70, <https://doi.org/10.1016/j.marchem.2019.03.001>, 2019.

1241

1242 Rantanen, M., Karpechko, A. Y., Lipponen, A., Nordling, K., Hyvärinen, O., Ruosteenoja, K.,
1243 Vihma, T., and Laaksonen, A.: The Arctic has warmed nearly four times faster than the globe
1244 since 1979, *Commun. Earth Environ.*, 3, 1–10, <https://doi.org/10.1038/s43247-022-00498-3>,
1245 2022.

1246

1247 Rheuban, J. E., Doney, S. C., McCorkle, D. C. and Jakuba, R. W. Quantifying the Effects of
1248 Nutrient Enrichment and Freshwater Mixing on Coastal Ocean Acidification. *Journal of*
1249 *Geophysical Research: Oceans* 124(12), 9085–9100,
1250 <https://doi.org/10.1029/2019JC015556>, 2019.

1251

1252 Rysgaard, S., Glud, R. N., Sejr, M. K., Bendtsen, J., and Christensen, P. B.: Inorganic carbon
1253 transport during sea ice growth and decay: A carbon pump in polar seas, *J. Geophys. Res.*, 112,
1254 C03016, <https://doi.org/10.1029/2006JC003572>, 2007.

1255

1256 Rysgaard, S., Glud, R. N., Lennert, K., Cooper, M., Halden, N., Leakey, R. J. G., Hawthorne, F.
1257 C., and Barber, D.: Ikaite crystals in melting sea ice – implications for pCO₂ and pH levels in
1258 Arctic surface waters, *The Cryosphere*, 6, 901–908, <https://doi.org/10.5194/tc-6-901-2012>, 2012.
1259
1260 Sakamoto, C. M., Johnson, K. S., and Coletti, L. J.: Improved algorithm for the computation of
1261 nitrate concentrations in seawater using an in situ ultraviolet spectrophotometer, *Limnol.*
1262 *Oceanogr. Methods*, 7, 132–143, <https://doi.org/10.4319/lom.2009.7.132>, 2009.
1263
1264 Sandy, S. J., Danielson, S. L., and Mahoney, A. R.: Automating the Acoustic Detection and
1265 Characterization of Sea Ice and Surface Waves, *J. Mar. Sci. Eng.*, 10, 1577,
1266 <https://doi.org/10.3390/jmse10111577>, 2022.
1267
1268 Sarmiento, J. L. and Gruber, N.: *Ocean Biogeochemical Dynamics*, Princeton University Press,
1269 Princeton, NJ, 526 pp., 2006.
1270
1271 Seabird. Application Note 31: Computing temperature and conductivity slope and offset
1272 correction coefficients from lab calibration and salinity bottle samples. [my.hach.com/asset-](http://my.hach.com/asset-get.download.jsa?id=54627861537)
1273 [get.download.jsa?id=54627861537](http://my.hach.com/asset-get.download.jsa?id=54627861537), accessed 20 June 2016.
1274
1275 Seabird. Module 28. Advanced Biogeochemical Processing, [www.seabird.com/cms-](http://www.seabird.com/cms-portals/seabird_com/cms/documents/training/Module28_Advanced_Biogeochem_Processing.pdf)
1276 [portals/seabird_com/cms/documents/training/Module28_Advanced_Biogeochem_Processing.pdf](http://www.seabird.com/cms/documents/training/Module28_Advanced_Biogeochem_Processing.pdf)
1277 . Accessed 30 May 2023.
1278

1279 Seferian, R.: CNRM-CERFACS CNRM-ESM2-1 model output prepared for CMIP6
1280 AerChemMIP. doi:10.22033/ESGF/CMIP6.1389, 2019.
1281
1282 Semiletov, I., Pipko, I., Gustafsson, Ö., Anderson, L. G., Sergienko, V., Pugach, S., Dudarev, O.,
1283 Charkin, A., Gukov, A., Bröder, L., Andersson, A., Spivak, E., and Shakhova, N.: Acidification
1284 of East Siberian Arctic Shelf waters through addition of freshwater and terrestrial carbon. *Nature*
1285 *Geosci* 9, 361–365, <https://doi.org/10.1038/ngeo2695>, 2016.
1286
1287 Serreze, M. C. and Barry, R. G.: Processes and impacts of Arctic amplification: A research
1288 synthesis, *Glob. Planet. Change*, 77, 85–96, <https://doi.org/10.1016/j.gloplacha.2011.03.004>,
1289 2011.
1290
1291 Serreze, M. C. and Francis, J. A.: The Arctic amplification debate, *Clim. Change*, 76, 241–264,
1292 <https://doi.org/10.1007/s10584-005-9017-y>, 2006.
1293
1294 Serreze, M. C., Crawford, A. D., Stroeve, J. C., Barrett, A. P., and Woodgate, R. A.: Variability,
1295 trends, and predictability of seasonal sea ice retreat and advance in the Chukchi Sea, *J. Geophys.*
1296 *Res. Oceans*, 121, 7308–7325, <https://doi.org/10.1002/2016JC011977>, 2016.
1297
1298 Sharp, J. D., Pierrot, D., Humphreys, M. P., Epitalon, J.-M., Orr, J. C., Lewis, E. R., and
1299 Wallace, D. W. R.: CO2SYSv3 for MATLAB, <https://doi.org/10.5281/zenodo.7552554>, 2023.
1300

1301 Shu, Q., Wang, Q., Årthun, M., Wang, S., Song, Z., Zhang, M., and Qiao, F: Arctic Ocean
1302 Amplification in a warming climate in CMIP6 models. *Science Advances*, 8(30), eabn9755.
1303 <https://doi.org/10.1126/sciadv.abn9755>, 2022.
1304
1305 Stabeno, P. J., Mordy, C. W. and Sigler, M. F.: Seasonal patterns of near-bottom chlorophyll
1306 fluorescence in the eastern Chukchi Sea: 2010–2019. *Deep Sea Research Part II: Topical Studies*
1307 *in Oceanography* 177, 104842, <https://doi.org/10.1016/j.dsr2.2020.104842>, 2020.
1308
1309 Stackpoole, S., Butman, D., Clow, D., Verdin, K., Gaglioti, B., and Striegl, R. G.: Carbon burial,
1310 transport, and emission from inland aquatic ecosystems in Alaska, *USGS Prof. Pap.*, 1826, 159–
1311 188, <https://doi.org/10.3133/pp1826>, 2016.
1312
1313 Stackpoole, S. M., Butman, D., Clow, D. W., Verdin, K. L., Gaglioti, B. V., Genet, H., and
1314 Striegl, R. G.: Inland waters and their role in the carbon cycle of Alaska, *Ecol. Appl.*, 27, 1403–
1315 1420, <http://onlinelibrary.wiley.com/doi/10.1002/eap.1552/full>, 2017.
1316
1317 Silvers, L., Blanton, C., McHugh, C., John, J. G., Radhakrishnan, A., Rand, K., Balaji, V.,
1318 Dupuis, C., Durachta, J., Guo, H., Hemler, R., Lin, P., Nikonov, S., Paynter, D. J., Ploshay, J.,
1319 Vahlenkamp, H., Wilson, C., Wyman, B., Robinson, T., Zeng, Y. and Zhao, M.: NOAA-GFDL
1320 GFDL-CM4 model output prepared for CMIP6 CFMIP. doi:10.22033/ESGF/CMIP6.1641, 2018.
1321

1322 Stroeve, J. C., Serreze, M. C., Holland, M. M., Kay, J. E., Malanik, J., and Barrett, A. P.: The
1323 Arctic's rapidly shrinking sea ice cover: a research synthesis, *Clim. Change*, 110, 1005–1027,
1324 <https://doi.org/10.1007/s10584-011-0101-1>, 2011.
1325
1326 Stroeve, J. C., Markus, T., Boisvert, L., Miller, J., and Barrett, A.: Changes in Arctic melt season
1327 and implications for sea ice loss, *Geophys. Res. Lett.*, 41, 1216–1225,
1328 <https://doi.org/10.1002/2013GL058951>, 2014.
1329
1330 Stumpp, M., Hu, M. Y., Melzner, F., Gutowska, M. A., Dorey, N., Himmerkus, N., Holtmann,
1331 W. C., Dupont, S. T., Thorndyke, M. C., and Bleich, M.: Acidified seawater impacts sea urchin
1332 larvae pH regulatory systems relevant for calcification, *Proc. Natl. Acad. Sci. USA*, 109, 18192–
1333 18197, <https://doi.org/10.1073/pnas.1209174109>, 2012.
1334
1335 Sulpis, O., Lauvset, S. K., and Hagens, M.: Current estimates of K_1^* and K_2^* appear inconsistent
1336 with measured CO_2 system parameters in cold oceanic regions, *Ocean Sci.*, 16, 847–862,
1337 <https://doi.org/10.5194/os-16-847-2020>, 2020.
1338
1339 Takahashi, T., Sutherland, S. C., Sweeney, C., Poisson, A., Metzl, N., Tilbrook, B., Bates, N.,
1340 Wanninkhof, R., Feely, R. A., Sabine, C., Olafsson, J., and Nojiri, Y.: Global sea–air CO_2 flux
1341 based on climatological surface ocean pCO_2 , and seasonal biological and temperature effects,
1342 *Deep Sea Res. Part II Top. Stud. Oceanogr.*, 49, 1601–1622, [https://doi.org/10.1016/S0967-](https://doi.org/10.1016/S0967-0645(02)00003-6)
1343 [0645\(02\)00003-6](https://doi.org/10.1016/S0967-0645(02)00003-6), 2002.
1344

1345 Terhaar, J., Torres, O., Bourgeois, T., and Kwiatkowski, L.: Arctic Ocean acidification over the
1346 21st century co-driven by anthropogenic carbon increases and freshening in the CMIP6 model
1347 ensemble, *Biogeosciences*, 18, 2221–2240, <https://doi.org/10.5194/bg-18-2221-2021>, 2021.
1348

1349 Thomsen, J., Casties, I., Pansch, C., Körtzinger, A., and Melzner, F.: Food availability outweighs
1350 ocean acidification effects in juvenile *Mytilus edulis*: laboratory and field experiments, *Glob.*
1351 *Change Biol.*, 19, 1017–1027, <https://doi.org/10.1111/gcb.12109>, 2013.
1352

1353 Thor, P. and Dupont, S.: Transgenerational effects alleviate severe fecundity loss during ocean
1354 acidification in a ubiquitous planktonic copepod, *Glob. Change Biol.*, 21, 2261–2271,
1355 <https://doi.org/10.1111/gcb.12815>, 2015.
1356

1357 Tian, F., Pickart, R.S., Lin, P., Pacini, A., Moore, G.W.K., Stabeno, P., Weingartner, T., Itoh,
1358 M., Kikuchi, T., Dobbins, E. and Bell, S.: Mean and seasonal circulation of the eastern Chukchi
1359 Sea from moored timeseries in 2013–2014. *Journal of Geophysical Research: Oceans*, 126(5),
1360 p.e2020JC016863, 2021.
1361

1362 Tunnicliffe, V., Davies, K. T. A., Butterfield, D. A., Embley, R. W., Rose, J. W., and Chadwick
1363 Jr, W. W.: Survival of mussels in extremely acidic waters on a submarine volcano, *Nat. Geosci.*,
1364 2, 344–348, <https://doi.org/10.1038/ngeo500>, 2009.
1365

1366 Van Straalen, M. N.: Peer Reviewed: Ecotoxicology Becomes Stress Ecology, *Environ. Sci.*
1367 *Technol.*, 37, 324A–330A, <https://doi.org/10.1021/es0325720>, 2003.

1368

1369 Vargas, C. A., Lagos, N. A., Lardies, M. A., Duarte, C., Manríquez, P. H., Aguilera, V. M.,
1370 Broitman, B., Widdicombe, S., and Dupont, S.: Species-specific responses to ocean acidification
1371 should account for local adaptation and adaptive plasticity, *Nat Ecol Evol* **1**, 0084,
1372 <https://doi.org/10.1038/s41559-017-0084>, 2017.

1373

1374 Vargas, C. A., Cuevas, L. A., Broitman, B. R., San Martin, V. A., Lagos, N. A., Gaitán-Espitia,
1375 J. D., and Dupont, S.: Upper environmental pCO₂ drives sensitivity to ocean acidification in
1376 marine invertebrates, *Nat. Clim. Change*, **12**, 200–207, [https://doi.org/10.1038/s41558-021-](https://doi.org/10.1038/s41558-021-01269-2)
1377 [01269-2](https://doi.org/10.1038/s41558-021-01269-2), 2022.

1378

1379 Ventura, A., Schulz, S., and Dupont, S.: Maintained larval growth in mussel larvae exposed to
1380 acidified under-saturated seawater, *Sci. Rep.*, **6**, 23728, <https://doi.org/10.1038/srep23728>, 2016.

1381

1382 Vergara-Jara, M. J., DeGrandpre, M. D., Torres, R., Beatty, C. M., Cuevas, L. A., Alarcón, E.
1383 and Iriarte, J. L.: Seasonal Changes in Carbonate Saturation State and Air-Sea CO₂ Fluxes During
1384 an Annual Cycle in a Stratified-Temperate Fjord (Reloncaví Fjord, Chilean Patagonia). *Journal*
1385 *of Geophysical Research: Biogeosciences* **124**, 2851–2865,
1386 <https://doi.org/10.1029/2019JG005028>, 2019.

1387

1388 Watanabe, Y. W., Li, B. F., Yamasaki, R., Yunoki, S., Imai, K., Hosoda, S., and Nakano, Y.:
1389 Spatiotemporal changes of ocean carbon species in the western North Pacific using

1390 parameterization technique, *J. Oceanogr.*, 76, 155–167, <https://doi.org/10.1007/s10872-019->
1391 00532-7, 2020.

1392

1393 Williams, N. L., Juranek, L. W., Johnson, K. S., Feely, R. A., Riser, S. C., Talley, L. D., Russell,
1394 J. L., Sarmiento, J. L., and Wanninkhof, R.: Empirical algorithms to estimate water column pH
1395 in the Southern Ocean, *Geophys. Res. Lett.*, 43, 3415–3422,
1396 <https://doi.org/10.1002/2016GL068539>, 2016.

1397

1398 Wieners, K.-H., Giorgetta, M., Jungclaus, J., Reick, C., Esch, M., Bittner, M., Legutke, S.,
1399 Schupfner, M., Wachsmann, F., Gayler, V., Haak, H., de Vrese, P., Raddatz, T., Mauritsen, T.,
1400 von Storch, J.-S., Behrens, J., Brovkin, V., Claussen, M., Crueger, T., Fast, I., Fiedler, S.,
1401 Hagemann, S., Hohenegger, C., Jahns, T., Kloster, S., Kinne, S., Lasslop, G., Kornblueh, L.,
1402 Marotzke, J., Matei, D., Meraner, K., Mikolajewicz, U., Modali, K., Müller, W., Nabel, J., Notz,
1403 D., Peters-von Gehlen, K., Pincus, R., Pohlmann, H., Pongratz, J., Rast, S., Schmidt, H., Schnur,
1404 R., Schulzweida, U., Six, K., Stevens, B., Voigt, A. and Roeckner, E.: MPI-M MPI-ESM1.2-LR
1405 model output prepared for CMIP6 CMIP historical. doi:10.22033/ESGF/CMIP6.6595, 2019.

1406

1407 Wolf-Gladrow, D. A., Zeebe, R. E., Klaas, C., Körtzinger, A., and Dickson, A. G.: Total
1408 alkalinity: The explicit conservative expression and its application to biogeochemical processes,
1409 *Mar. Chem.*, 106, 287–300, <https://doi.org/10.1016/j.marchem.2007.01.006>, 2007.

1410

1411 Wood, K. R., Bond, N. A., Danielson, S. L., Overland, J. E., Salo, S. A., Stabeno, P. J., and
1412 Whitefield, J.: A decade of environmental change in the Pacific Arctic region, *Prog. Oceanogr.*,
1413 136, 12–31, <https://doi.org/10.1016/j.pocean.2015.05.005>, 2015.
1414
1415 Woosley, R. J.: Evaluation of the temperature dependence of dissociation constants for the
1416 marine carbon system using pH and certified reference materials, *Marine Chemistry*,
1417 229, 103914, <https://doi.org/10.1016/j.marchem.2020.103914>, 2021.
1418
1419 Woosley, R. J., Millero, F. J., and Takahashi, T.: Internal consistency of the inorganic carbon
1420 system in the Arctic Ocean, *Limnol. Oceanogr. Methods*, 15, 887–896,
1421 <https://doi.org/10.1002/lom3.10208>, 2017.
1422
1423 Woosley, R. J. and Millero, F. J.: Freshening of the western Arctic negates anthropogenic carbon
1424 uptake potential, *Limnol. Oceanogr.*, 65, 1834–1846, <https://doi.org/10.1002/lno.11421>, 2020.
1425
1426 Yamamoto-Kawai, M., McLaughlin, F. A., Carmack, E. C., Nishino, S., and Shimada, K.:
1427 Aragonite undersaturation in the Arctic Ocean: effects of ocean acidification and sea ice melt,
1428 *Science*, 326, 1098–1100, <https://doi.org/10.1126/science.1174190>, 2009.
1429
1430 Zeng, J., Chen, M., Zheng, M., Hu, W., and Qiu, Y.: A potential nitrogen sink discovered in the
1431 oxygenated Chukchi Shelf waters of the Arctic, *Geochem. Trans.*, 18, 5,
1432 <https://doi.org/10.1186/s12932-017-0043-2>, 2017.
1433
1434

1435 **Tables**

1436 **Table 1.** Chukchi Ecosystem Observatory location and instrument sampling frequency. Sensor
 1437 type and parameter measured (italicized) shown in top row. Values in parenthesis indicate the
 1438 number of measurements averaged over the measurement interval window.

Deployment	Latitude	Longitude	SUNA <i>NO₃</i>	HydroC CO ₂ <i>pCO₂</i>	SBE16 <i>CTD+</i>	SBE37 <i>CTD</i>	SeaFET <i>pH</i>	SBE63 <i>O₂</i>
2016-2017	71°35'58.5600"N	161°31'06.2400"W	1 h	12 h (300/5 min)*	1 h	-	-	-
2017-2018	71°35'58.9200"N	161°31'08.0400"W	1 h	12 h (5/5 min)	2 h	2 h	2 h (30/5 min)	2 h
2018-2019	71°35'59.6400"N	161°31'41.1600"W	1 h	24 h (5/5 min)	1 h	2 h*	-	2 h*
2019-2020	71°35'58.9200"N	161°31'39.0000"W	1 h	12 h (5/5 min)	2 h	-	-	-

* indicates the sensor did not return data over the whole year due to battery failure
 CTD+ indicates ancillary data was available with the SBE16 file (e.g., chlorophyll fluorescence)

1439

1440

1441

1442 **Table 2.** Evaluation of pH_{SeaFET} and pH^{est} using reference pH from nearby discrete samples

1443 (pH^{disc}_{calc}). Uncertainty, u_c, is the propagated combined standard uncertainty from *errors.m* (Orr

1444 et al., 2018). pH_{SeaFET} and pH^{est} were interpolated to the discrete timestamp. Figure S1 for

1445 visualization of reference values.

1446

Date	Cruise	Cast No.	Distance (km)	pH ^{disc} _{calc} ± u _c	Anomaly (pH ^{est} -pH ^{disc} _{calc})	Anomaly (pH _{SeaFET} -pH ^{disc} _{calc})	Source
------	--------	----------	------------------	---	---	--	--------

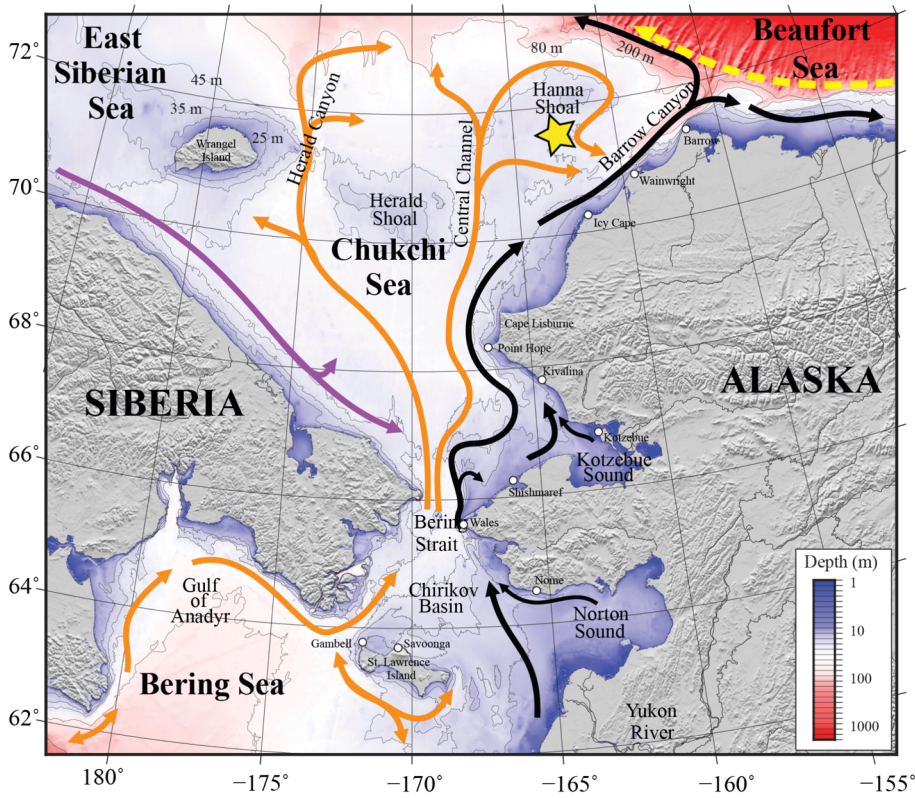
Formatted: Subscript
 Formatted Table
 Deleted: -161.5184
 Formatted: Font: Times New Roman, 10 pt
 Formatted: Font: 10 pt
 Formatted: Font: Times New Roman, 10 pt
 Formatted: Font color: Auto
 Deleted: 71.5996
 Formatted: Font color: Auto
 Formatted: Normal, Left, Indent: Left: 0", Line spacing: single
 Deleted: -161.5189
 Formatted: Font: Times New Roman, 10 pt
 Formatted: Font: 10 pt
 Formatted: Font: Times New Roman, 10 pt
 Formatted: Normal, Left, Indent: Left: 0", Line spacing: single
 Formatted: Font color: Auto
 Deleted: 71.5997
 Deleted: -161.5281
 Formatted: Font: Times New Roman, 10 pt
 Formatted: Font: 10 pt
 Formatted: Font: Times New Roman, 10 pt
 Formatted: Font color: Auto
 Formatted: Normal, Left, Indent: Left: 0", Line spacing: single
 Deleted: 71.5999
 Formatted: Left, Indent: Left: 0"
 Deleted: 71.5997
 Deleted: -161.5275
 Formatted: Font: Times New Roman, 10 pt
 Formatted: Font color: Auto
 Formatted: Font: Times New Roman, 10 pt
 Formatted: Font color: Auto
 Formatted: Normal, Left, Indent: Left: 0", Line spacing: single

2017-09-10	HLY1702	127	0.52	8.0123±0.0166	-0.0450*	-0.0354	Cross et al., 2020a
2019-08-11	HLY1901	39	3.75	7.6423±0.012	0.0079*	-	Cross et al., 2021
2019-08-19	OS1901	33	0.27	7.7367±0.0145	-0.0200	-	unpublished

* indicates $\text{pH}^{\text{disc}}_{\text{calc}}$ was interpolated to mooring depth

1455

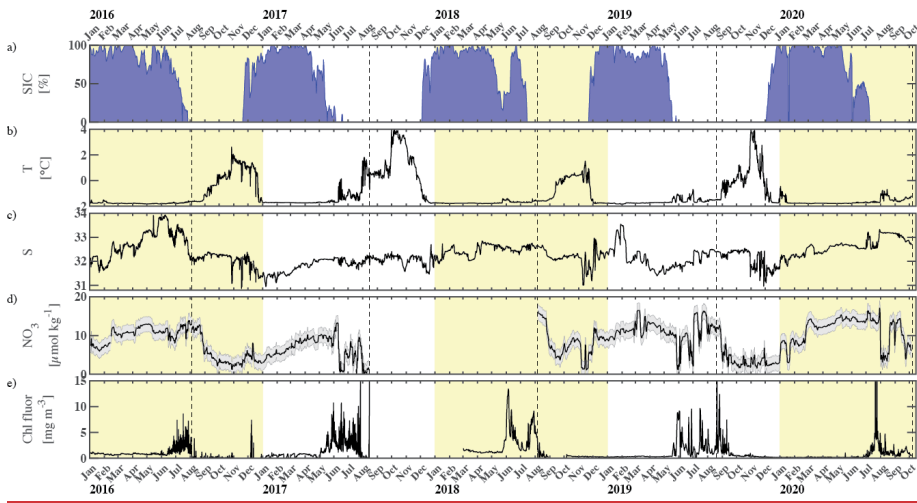
1456



1458
 1459 **Figure 1. Map of the study area.** Bathymetry of the Chukchi, northern Bering, East Siberian
 1460 and eastern Beaufort seas is shown in color. The Chukchi Ecosystem Observatory (CEO)
 1461 location near Hanna Shoal is marked with a yellow star. General circulation patterns are shown
 1462 with arrows: black – Alaskan Coastal Water and Alaskan Coastal Current, dividing into the
 1463 Shelf-break Jet (right) and Chukchi Slope Current (left, Corlett and Pickart, (2017)); orange –
 1464 Anadyr, Bering, and Chukchi Seawater; purple – Siberian Coastal Current; yellow – Beaufort
 1465 Gyre boundary current. Figure is from Hauri et al. (2018).

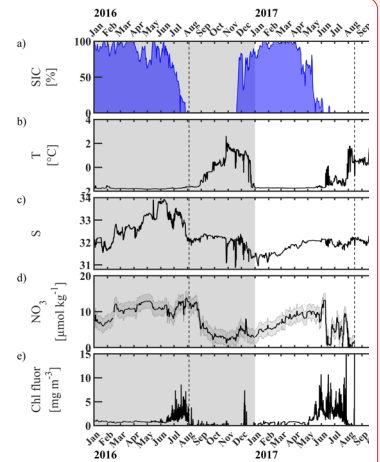
1466

1467

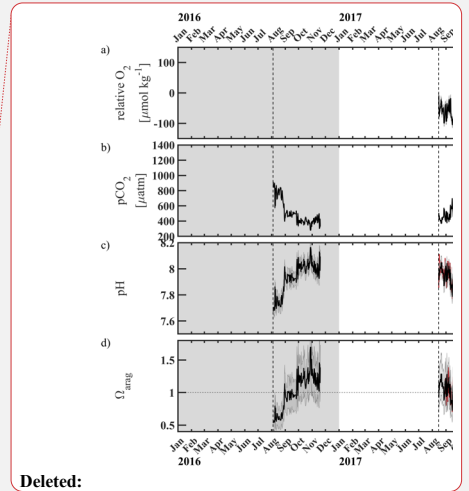
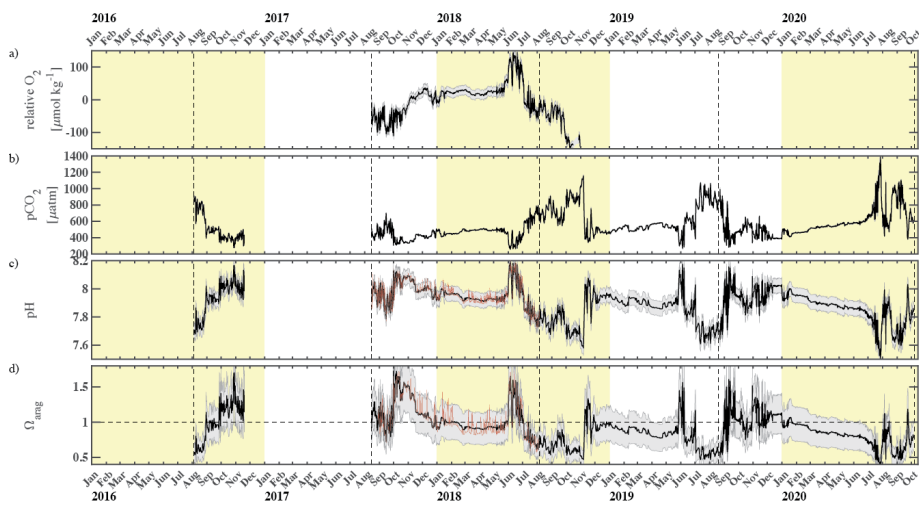


1468

1469 **Figure 2. Chukchi Ecosystem Observatory timeseries from 2016 through 2020.** a) sea ice
1470 concentration (blue shading to highlight coverage, %; DiGirolamo et al., 2022), b) temperature
1471 (°C), c) salinity, d) NO₃ with uncertainty envelope ($\mu\text{mol kg}^{-1}$), and e) chlorophyll fluorescence
1472 (mg m^{-3}). Years are indicated by alternating yellow and white background shading. The vertical
1473 dotted gray lines indicate the mooring turn around timing.



Deleted:
Deleted: gray



Deleted:

Deleted: gray

1476

1477 **Figure 3. Chukchi Ecosystem Observatory timeseries from 2016 through 2020, part 2. a)**

1478 relative dissolved oxygen with uncertainty envelope (relative to the mean; $\mu\text{mol kg}^{-1}$), b) $p\text{CO}_2$

1479 with uncertainty envelope (μatm ; Hauri and Irving, 2023a), c) pH with uncertainty envelope

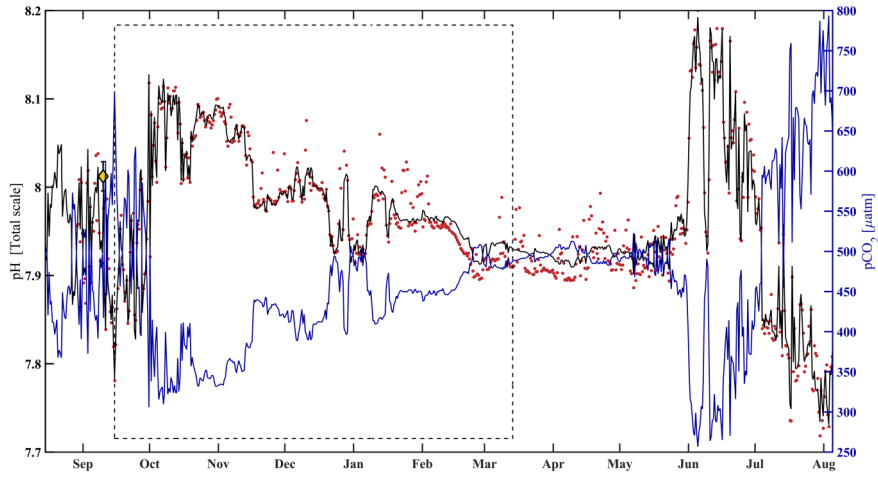
1480 (pH^{est} in black, $\text{pH}^{\text{SeaFET}}$ in red; Hauri and Irving 2023b), and d) aragonite saturation state with

1481 uncertainty envelope ($\Omega_{\text{arag}}(p\text{CO}_2, \text{pH}^{\text{est}})$ in black; $\Omega_{\text{arag}}(p\text{CO}_2, \text{pH}^{\text{SeaFET}})$ in red). Years are

1482 indicated by alternating **yellow** and white backgrounds. The vertical dotted gray lines indicate

1483 the mooring turn around timing.

1484



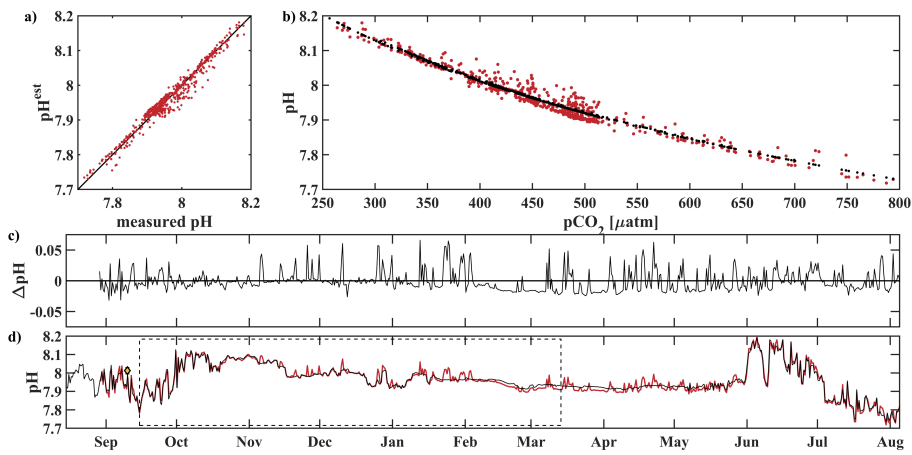
1487

1488

1489 **Figure 4. HydroC $p\text{CO}_2$ and pH highlighting mirrored trend from mid-August 2017 to**
 1490 **beginning of August 2018.** Measured pH ($\text{pH}_{\text{SeaFET}}$, red dots) is interpolated onto the HydroC
 1491 $p\text{CO}_2$ timestamp (blue), and pH^{est} is shown as the solid black line. The dashed box shows the
 1492 period over which pH^{est} was trained. The yellow faced diamond with error bars show reference
 1493 $\text{pH}^{\text{disc}}_{\text{calc}} \pm u_c$ (Table 2; Cross et al., 2020a; Orr et al., 2018).

1494

1495

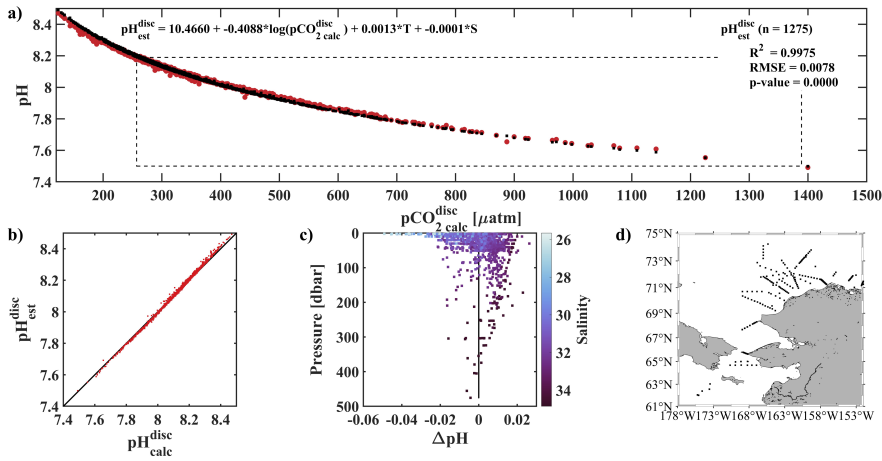


1496

1497 **Figure 5. Performance of the pH algorithm.** (a) pH_{SeaFET} vs pH^{est} with black line highlighting
1498 1:1 ratio, (b) pCO_2 vs pH_{SeaFET} (red) and pCO_2 vs pH^{est} (black), (c) residual pH (pH_{SeaFET} -
1499 pH^{est}), and (d) pH_{SeaFET} (red) and pH^{est} (black) vs. time, with dashed box highlighting the period
1500 over which pH^{est} was trained (15 September - 14 March 2017), and the yellow faced diamond
1501 with error bars showing reference $pH^{disc}_{calc} \pm u_c$ (Table 2; Cross et al., 2020).

1502

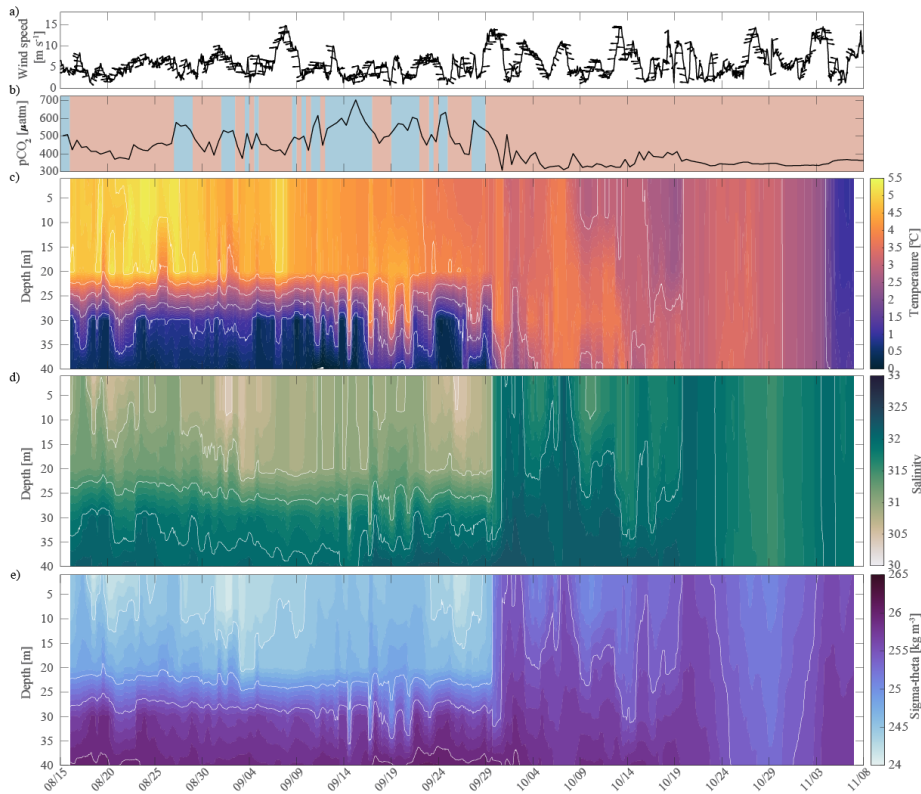
1503
1504
1505



1506

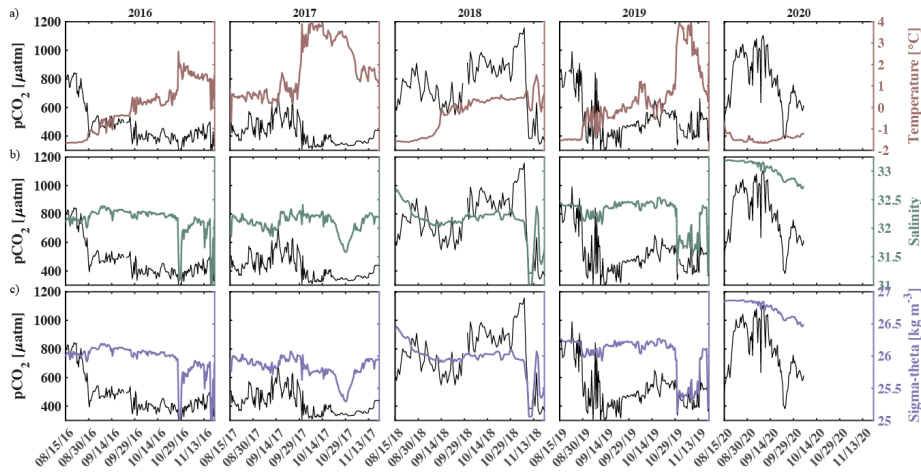
1507 **Figure 6. Evaluation of the pH algorithm.** pH^{est} evaluation with $\text{pH}^{\text{disc}}_{\text{calc}}$ from discrete
1508 samples collected during 4 cruises in the fall or early winter (August - November) of 2017-2020
1509 and $\text{pH}^{\text{disc}}_{\text{est}}$ from our linear regression model (Equation 2). (a) $p\text{CO}_2^{\text{disc}}_{\text{calc}}$ (TA, DIC) vs pH (red
1510 $\text{pH}^{\text{disc}}_{\text{calc}}$ and black $\text{pH}^{\text{disc}}_{\text{est}}$) with dashed black box showing the range of pH and $p\text{CO}_2$ observed
1511 at the CEO at 33 m depth, (b) $\text{pH}^{\text{disc}}_{\text{calc}}$ vs $\text{pH}^{\text{disc}}_{\text{est}}$ with black 1:1 ratio, (c) residual pH ($\text{pH}^{\text{disc}}_{\text{calc}}$ -
1512 $\text{pH}^{\text{disc}}_{\text{est}}$) vs depth with color shading by salinity and black vertical line at 0, and (d) map showing
1513 the locations of the 1275 discrete water samples used for evaluation (Monacci et al., 2022; Cross
1514 et al., 2021; 2020a; 2020b).

1515
1516



1517

1518 **Figure 7. Water column structure from late summer 2017 to freeze up.** Profiles of a) wind
 1519 speed and direction (arrows pointing downwind) from the NOAA-operated Wiley Post-Will
 1520 Rogers Memorial Airport, b) $p\text{CO}_2$ (μatm) with blue background indicating the water was
 1521 undersaturated regarding aragonite ($\Omega_{\text{arag}} < 1$) and red shading indicating aragonite
 1522 oversaturation ($\Omega_{\text{arag}} \geq 1$), c) temperature ($^{\circ}\text{C}$), d) salinity, and e) sigma-theta (kg m^{-3}).
 1523 Temperature (c) and salinity (d) were measured at 8, 20, 30, and 40 m by the Chukchi Ecosystem
 1524 Observatory freeze-up detection mooring deployed in fall 2017. Density was calculated with the
 1525 TEOS-10 GSW Oceanographic Toolbox (McDougall and Baker, 2011).



1526

1527 **Figure 8. Impact of water column mixing on $p\text{CO}_2$.** Timeseries of $p\text{CO}_2$ (black, left axis) and
 1528 a) temperature (maroon, right axis), b) salinity (green, right axis), and c) density (purple, right
 1529 axis) for 15 August to 1 December in 2016 -2020 measured at ~33m septh at the Chukchi Sea
 1530 Ecosystem Observatory.

1531

1532

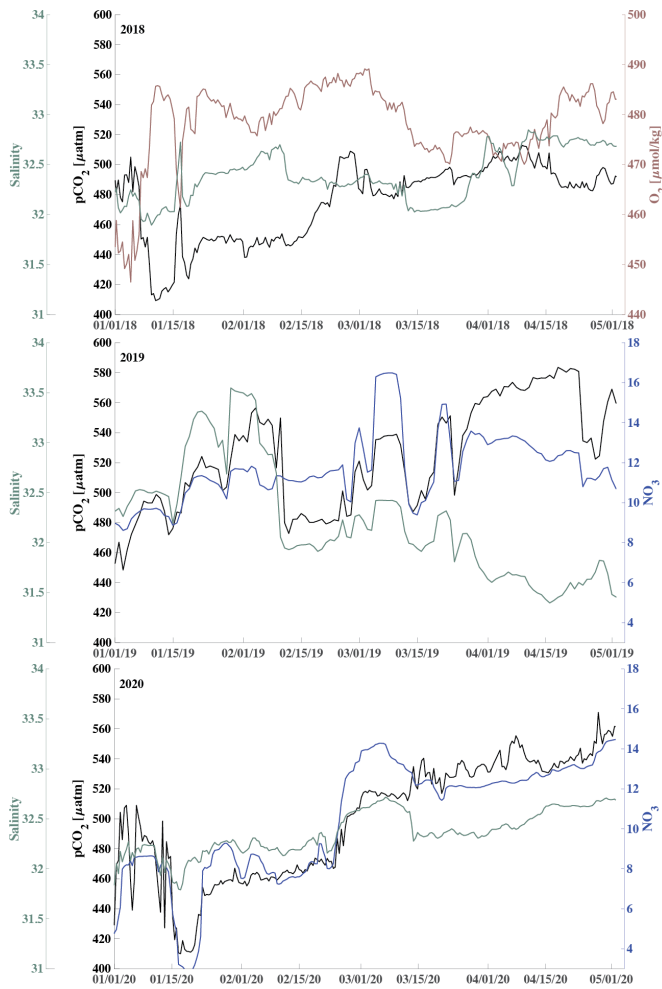
1533

1534

1535

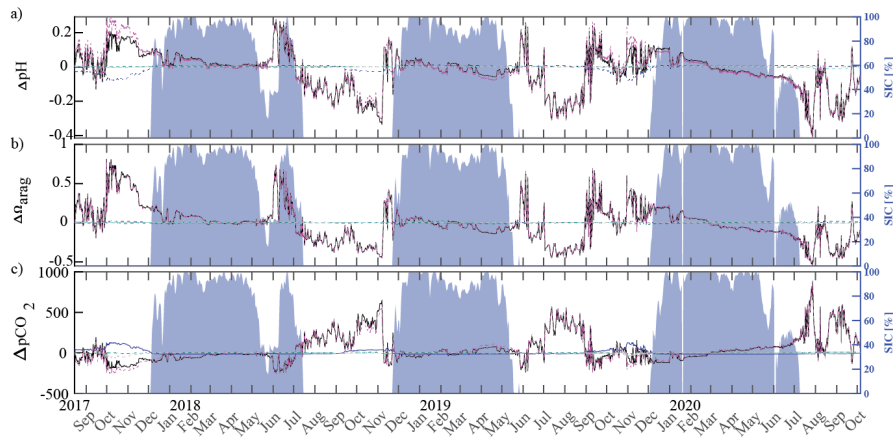
1536

1537



1538

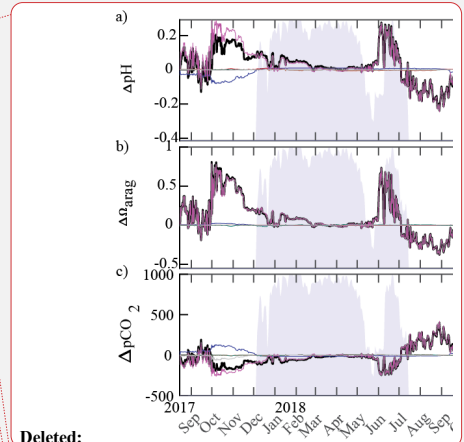
1539 **Figure 9. Respiration under the sea ice.** Timeseries of $p\text{CO}_2$ (black) and salinity (green, left
 1540 axis), and oxygen (O_2 , $\mu\text{mol kg}^{-1}$, maroon, top) and nitrate (NO_3 , $\mu\text{mol kg}^{-1}$, blue, middle and
 1541 bottom) concentration (right axis during January through April for 2018 (top), 2019 (middle) and
 1542 2020 (bottom).



1543

1544 **Figure 10. Drivers of the inorganic carbon system.** Component timeseries of the linear Taylor
 1545 decomposition of a) pH, b) Ω_{arag} , and c) pCO_2 . Contributions of changes in salinity (red),
 1546 temperature (blue), biogeochemistry (pink), and freshwater mixing (green) to changes (black,
 1547 relative to the mean of the timeseries) in pH, Ω_{arag} , and pCO_2 were computed following Rheuban
 1548 et al. (2019). The grey dotted line illustrates an estimated residual term. Sea ice concentration
 1549 (blue shading, %; DiGirolamo et al., 2022) is shown on the right axes.

1550

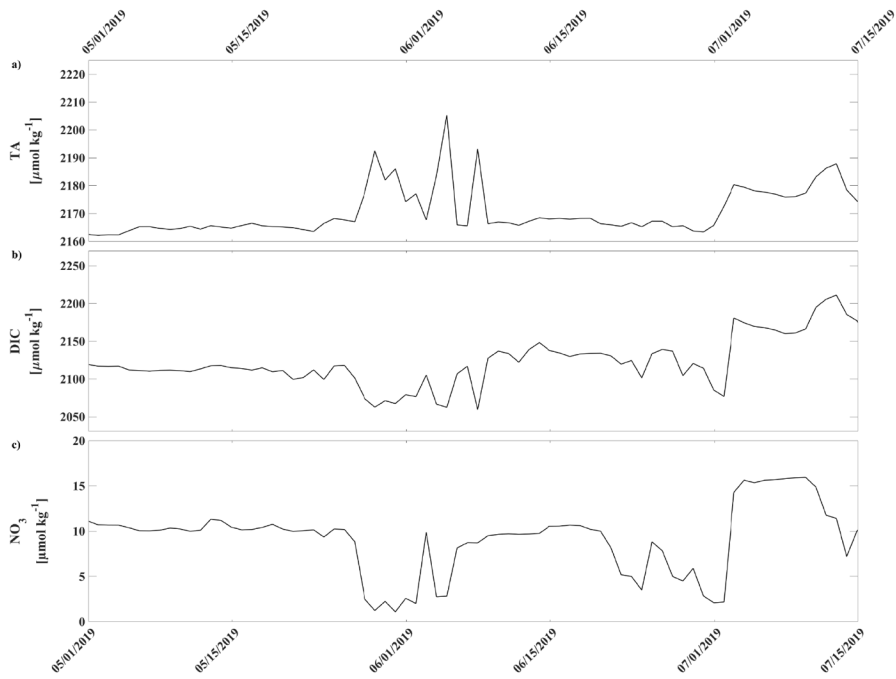


Deleted:

Deleted: The perturbation effects due to

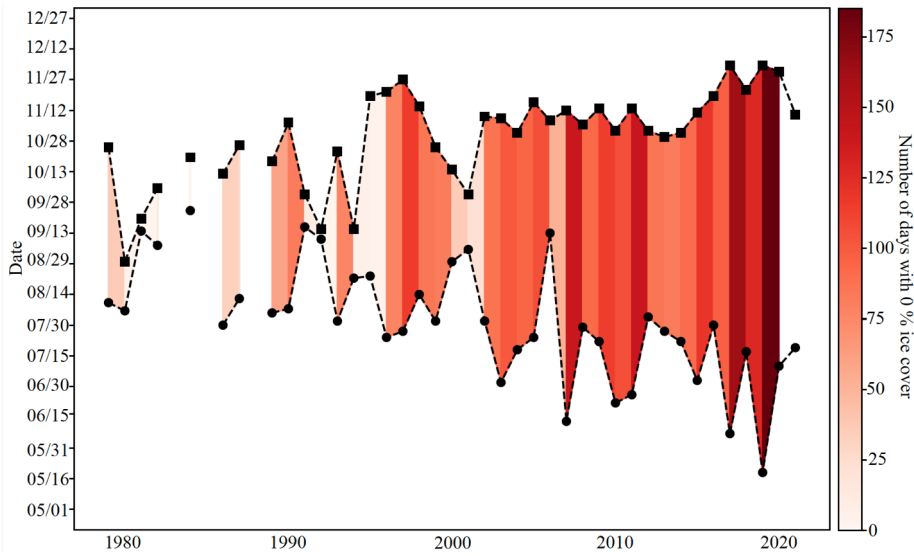
Deleted: , and an estimated residual term (grey)

Deleted:



1555

1556 **Figure 11. Spring 2019 relaxation event.** Timeseries of a) total alkalinity (TA, $\mu\text{mol kg}^{-1}$), b)
 1557 dissolved inorganic carbon (DIC, $\mu\text{mol kg}^{-1}$), and c) nitrate (NO_3 , $\mu\text{mol kg}^{-1}$) from May 1st, 2019
 1558 through July 15th, 2019.



1559

1560

1561 **Figure 12. Low sea ice period at the Chukchi Sea Observatory.** Timeseries of start (circle)

1562 and end (square) of low sea ice (< 15 % per grid cell) period from 1982-2021. Shades of red

1563 illustrate number of days with 0 % sea ice cover. The satellite sea ice cover at the observatory

1564 site was taken from the NSIDC (DiGirolamo et al., 2022).

1565